# Observations and Numerical Simulations of the Onset and Growth of Langmuir Circulations

ALEXANDER ANDRIATIS,[a] LUC LENAIN,[a] MATTHEW H. ALFORD,[a] NATHANIEL WINSTEAD,[b] AND JOSEPH GEIMAN[b]

[a] *Scripps Institution of Oceanography, La Jolla, California*
[b] *Johns Hopkins Applied Physics Laboratory, Laurel, Maryland*

(Manuscript received 9 January 2024, in final form 26 April 2024, accepted 8 May 2024)

ABSTRACT: We report novel observations of the onset and growth of Langmuir circulations (LCs) from simultaneous airborne and subsurface in situ measurements. Under weak, fetch-limited wind–wave forcing with stabilizing buoyancy forcing, the onset of LCs is observed for wind speeds greater than about 1 m $s^{-1}$. LCs appear nonuniformly in space, consistent with previous laboratory experiments and suggestive of coupled wave–turbulence interaction. Following an increase in wind speed from <1 m $s^{-1}$ to sustained 3 m $s^{-1}$ winds, a shallow (<0.7 m) diurnal warm layer is observed to deepen at 1 m $h^{-1}$, while the cross-cell scales of LCs grow at 2 m $h^{-1}$, as observed in sea surface temperature collected from a research aircraft. Subsurface temperature structures show temperature intrusions into the base of the diurnal warm layer of the same scale as bubble entrainment depth during the deepening period and are comparable to temperature structures observed during strong wind forcing with a deep mixed layer that is representative of previous LC studies. We show that an LES run with observed initial conditions and forcing is able to reproduce the onset and rate of boundary layer deepening. The surface temperature expression however is significantly different from observations, and the model exhibits large sensitivity to the numerical representation of surface radiative heating. These novel observations of Langmuir circulations offer a benchmark for further improvement of numerical models.

SIGNIFICANCE STATEMENT: The purpose of this study is to better understand the structure and dynamics of Langmuir circulations (LCs), coherent turbulent vortices in the surface ocean. Using observations of the ocean surface boundary layer from aircraft and autonomous instruments, we show the onset and growth of LCs. We compare the observations to a numerical model and find that while the model can reproduce the deepening of a shallow surface warm layer, the representation of coherent vortices differs from observations. Future studies can improve on the numerical representation of coherent upper ocean structures which are important to modeling upper ocean turbulence, air–sea exchanges, biology, ocean acoustics, and the distribution of anthropogenic pollutants like oil and microplastics.

KEYWORDS: Atmosphere-ocean interaction; Turbulence; Langmuir circulation; Aircraft observations; In situ oceanic observations; Large eddy simulations

## 1. Introduction

The ocean surface boundary layer (OSBL) connects the atmosphere to the ocean, mediating the transfer of energy, momentum, and gases, exchanges which are crucial in governing Earth's climate. The rate of air–sea exchange is driven by turbulence resulting from wind, wave, and buoyancy forcing (Fox-Kemper et al. 2022). Early efforts to understand mixing in the OSBL centered on shear instability forced by wind stress and convective instability from surface heat fluxes (Large et al. 1994). Wind-driven surface waves were found to influence mixing through wave breaking and Langmuir turbulence (LT) (D'Asaro et al. 2014; Sutherland and Melville 2015). LT is generated by the interaction of horizontally sheared surface currents with the Stokes drift of surface gravity waves. The vertical shear resulting from Stokes drift tilts vertical vorticity created by surface currents in the direction of wave propagation, creating wind-aligned roll vortices, a process known as the CL2 mechanism (Craik and Leibovich 1976). Pairs of vortices are spaced at regular intervals with a separation of about two times the boundary layer depth, forming coherent dynamical structures called Langmuir circulations (LCs) (Thorpe 2004). At the surface, pairs of roll vortices form convergence zones which concentrate buoyant particles such as algae or bubbles into elongated windrows, the commonly recognized surface expression of LCs (Langmuir 1938; Farmer and Li 1995). Below these convergence rows, subduction can entrain particles (Weller et al. 1985) but also plays an important role in momentum transfer from the surface, enhancing Eulerian shear and turbulent kinetic energy (TKE) at the base of the boundary layer (Li et al. 1995; Kukulka et al. 2010). Advancing our understanding of coherent LC structure can improve modeling of OSBL processes, such as the interaction of LCs with internal waves (Chini and Leibovich 2003) or fronts (Sullivan and McWilliams 2017), the scattering of sound of bubbles near the surface (Thorpe et al. 2003a), the dispersion of buoyant particles such as oil spills (Simecek-Beatty and Lehr 2017), biology (Larson 1992; Dierssen et al. 2015), and plastics (Cózar et al. 2021; Sutherland et al. 2023), the formation of sea ice (Drucker et al. 2003;

Denotes content that is immediately available upon publication as open access.

*Corresponding author*: Alexander Andriatis, aandriat@ucsd.edu

DOI: 10.1175/JPO-D-24-0004.1

Ciappa and Pietranera 2013), and applications to industry such as aquaculture (Yan et al. 2021) and wind power (Dorrell et al. 2022).

Langmuir turbulence is now understood to be a leading-order mixing process in the OSBL and needs to be included in global climate models, in particular, to improve mixed layer depth accuracy (Belcher et al. 2012). Early parameterizations of LT related TKE production to idealized parameters of wind stress and surface Stokes drift through the turbulent Langmuir number (McWilliams and Sullivan 2000). Including effects such as wind–wave misalignment and varying wave states has led to improvements in its parameterization (Smyth et al. 2002; Li et al. 2017; Li and Fox-Kemper 2017; Solano and Fan 2022). Including a parameterization of LT in regional (Schultz et al. 2020) and global ocean models (Li et al. 2017; Li and Fox-Kemper 2017) has significant impacts on mixed layer depth and can affect long-term ocean and climate trends (Li et al. 2016; Ali et al. 2019), but large differences due to model specifics need to be resolved, especially during mixed layer deepening and strong diurnal forcing (Li et al. 2019; Pham et al. 2023; Johnson et al. 2023).

Studies of LT behavior have primarily relied on large-eddy simulation (LES) models with CL2 vortex forcing (Skyllingstad and Denbo 1995; McWilliams et al. 1997). While early LES was largely used to model an idealized ocean, advances in understanding processes which impact LT scaling were made by simulating increasingly realistic ocean conditions, such as varying the decay scale of the Stokes drift (Harcourt and D'Asaro 2008) and changing the wind and wave directional alignment (Van Roekel et al. 2012; McWilliams et al. 2014; Wang et al. 2019). To further enhance realism, recent LES studies have run simulations with observed ocean and atmospheric conditions. Kukulka et al. (2009) find that LES reproduces mixed layer deepening and LC scale growth seen by Smith (1992) during a wind forcing event only when including LC effects. Kukulka et al. (2010) find that LT can enhance TKE production due to Stokes drift shear in the middle of the mixed layer, and the downwelling transfer of horizontal momentum interacts with the base of the thermocline, enhancing shear-driven instabilities and associated mixing. By comparing observations with wind–wave misalignment and fetch-limited winds, Fan et al. (2020) find that LT can lead to a TKE reduction in a swell-dominated wave field with underdeveloped wind seas by reducing shear production, and Wang et al. (2022) find reduced LT strength for fetch-limited winds, with less organized coherent LCs for misaligned wind and waves.

Few LES studies have modeled LT under stabilizing surface buoyancy forcing, in part because of the fine vertical grid spacing required to resolve turbulence for the shallowest diurnal warm layers (Beare et al. 2006). Min and Noh (2004) and Noh et al. (2009) show that LCs are important for the formation of a diurnal warm layer (DWL), but that sufficiently strong buoyancy forcing can inhibit LC formation. Conversely, Kukulka et al. (2013) show that sufficiently strong LT can inhibit diurnal restratification. Pearson et al. (2015) find a scaling for the boundary layer depth under stabilizing surface buoyancy forcing that is set by the initial mixed layer depth under equilibrium wind seas and the relative strength of buoyancy to wave forcing. Their simulations, however, do not account for changing wind forcing or for shallow diurnal warm layers under strongly stabilizing forcing whose depth is comparable to the Stokes drift decay scale. Wang et al. (2023) further develop boundary layer depth scaling that depends on wave, wind, and buoyancy forcing. Pham et al. (2023) demonstrate the importance of LT interacting with diurnal buoyancy forcing in LES studies of mixed layer behavior of monsoon intraseasonal oscillations.

In laboratory studies, LCs were generated shortly after the appearance of surface waves, on a time scale associated with the acceleration of a surface shear layer (Melville et al. 1998; Veron and Melville 2001). Recent experiments show that the onset of instability leading to Langmuir turbulence is sensitive to wave conditions, making wave-averaged LES models limited by their inability to capture the coupling between Langmuir turbulence and the surface wave field (Wagner et al. 2023). To properly represent LCs in models, parameterizations and LES need to be validated with observations across a variety of ocean and atmospheric conditions.

In situ ocean observations of Langmuir circulations come from a handful of experiments across a relatively narrow range of wind and buoyancy forcing regimes, and few have characterized both the lateral and vertical structure of coherent vortices. Weller and Price (1988) observed the three-dimensional flow structure of Langmuir circulations using buoyant drifters in combination with vector current meters deployed from R/P *Floating Instrument Platform* (*FLIP*). In regions of convergent surface flow, downward vertical and downwind horizontal velocities were observed of similar magnitude, with a subsurface maximum in the downwind jet. Sidescan sonar imaging of bubble clouds can provide a two-dimensional sonar image over a limited range, revealing the shape of convergence and downwelling zones where bubbles are entrained (Zedel and Farmer 1991; Farmer and Li 1995). Smith (1992) used surface velocity from sidescan sonar to trace the growth of LCs, finding that streak spacing between pairs of convergent bubble entrainment regions grew at about twice the rate of the deepening of the mixed layer, indicating a cell aspect ratio of about 1:1. Plueddemann et al. (1996) found a hierarchy of LC spacing over a broad wavenumber range (10–200 m) and a dependence of LC strength on both wind friction and Stokes drift magnitude in support of turbulent Langmuir number scaling (McWilliams et al. 1997). More recently, Chang et al. (2019) measured the cross-cell separation scale of Langmuir circulations using optically tracked bamboo surface drifters, finding a hierarchy of LC spacing. Temperature patterns can also be used to identify convergence and downwelling zones. At the surface, upwelling areas of LCs break the cool skin, leading to a cold signature in regions of convergence and downwelling (Veron et al. 2008a). Veron et al. (2009) showed the correlation between temperature structures of cool jets with broader warm patches and a surface velocity field consistent with Langmuir circulations using infrared (IR) imagery with particle image velocimetry. Airborne IR imagery has also been used for fine spatial and temperature resolution measurements of surface skin temperature (Zappa and Jessup 2005). Marmorino et al. (2005, 2007,

2008) used airborne IR to identify Langmuir circulations over a large area but lacked subsurface measurements to relate cell spacing to the boundary layer depth.

The goals of this study are to characterize the three-dimensional scales of LCs and the ocean and atmospheric forcing that governs their time evolution and to evaluate the ability of an LES forced from observations to reproduce the observed structure of LCs. We present the first simultaneous airborne and subsurface measurements of a wind forcing event leading to the onset of Langmuir circulations, allowing us to relate the surface cell structure to subsurface temperature patterns and boundary layer deepening. We collected data offshore of the Southern California coast in November 2020. Observations in the Catalina basin were characterized by a period of relatively low winds, small waves, and a shallow DWL with daytime heating and nightly cooling of the ocean surface. The onset of LCs was observed from airborne infrared imagery of sea surface temperature during a morning land breeze, followed by a stronger afternoon sea breeze that led to boundary layer deepening and growth of larger LCs, observed by airborne IR and thermistor chains on autonomous wave gliders. During a wind event further offshore with a deeper mixed layer, we observe similar subsurface temperature structures. We contextualize the wind, wave, and buoyancy forcing during our observations with nondimensional scale analysis. We compare our observations to an LES model initialized by observed ocean and atmospheric conditions and forced with observed wind and buoyancy forcing, with a Stokes drift parameterization based on the observed wind friction. In section 2, we review the experiment, instrumentation, and LES methodology. In section 3, we observe the onset and spatial structure of Langmuir circulations and compare them with an idealized LES run. In section 4, we observe the growth of LCs and deepening of the shallow surface warm layer under sustained wind forcing and compare surface and subsurface temperature structures with LES and with a more typical strong forcing regime. In section 5, we discuss and summarize the results.

## 2. Methods

### a. Experiment

The data used in this paper were collected as part of the Task Force Ocean (TFO) "Platform Centric ASW Processing with Through-the-Sensor Data Assimilation and Fusion" experiment off the coast of Southern California in November 2020 (https://doi.org/10.6075/J0VQ32W2; Andriatis et al. 2024). The experiment was conducted in two parts: a deployment in deep water (4 km, hereafter "offshore") between 5 and 14 November 2020 and a deployment in the Catalina basin between 15 and 24 November 2020. The deployments were based aboard the research vessel (R/V) *Sally Ride*, accompanied by numerous drifting instruments and remotely piloted wave gliders. During the Catalina deployment, the *Sally Ride* was joined by the R/V *Bob and Betty Beyster* and a fixed-wing aircraft. The *Beyster* provided assistance in repositioning assets as they drifted out of the operational region by

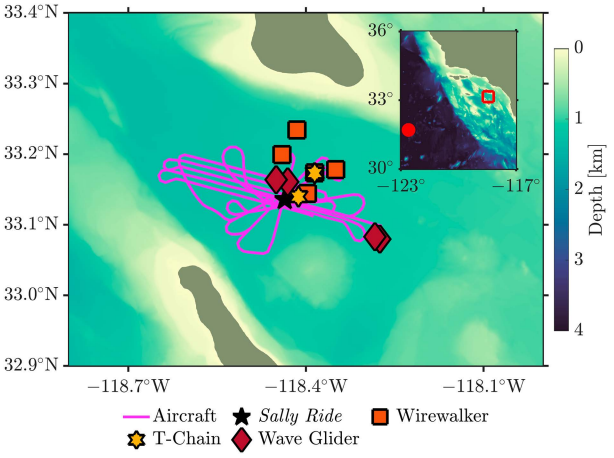


FIG. 1. Map showing the Catalina experiment region and deployed assets. The inset shows the larger California coast region, with the Catalina experiment area (red square outline) and the offshore experiment area (red circle). Aircraft tracks (pink) are plotted for flights from 1700 to 1800 UTC 20 Nov and 0000 to 0100 UTC 21 Nov. Asset locations are shown for their position at 2100 UTC 20 Nov.

strong along-channel currents, while the aircraft gathered aerial imagery of the ocean surface in transects over the experiment region. Figure 1 shows a snapshot of deployed assets in the Catalina basin, with an inset showing the larger California coast region and the offshore experiment site.

Because we are interested in observing how the scales of LCs evolve with changing atmospheric and ocean conditions, we focus on observing the evolution of LCs during and after a rapid increase in the wind stress on the ocean surface. Observations of wind during the experiment show a diurnal pattern of increased speeds during the afternoon sea breeze. The biggest relative increase in winds occurs on the afternoon of 20 November, with low winds of 1 m $s^{-1}$ during the day rapidly increasing to 5 m $s^{-1}$ into the evening (Fig. 2). For the majority of the analysis, we will focus on the time period from 1500 UTC 20 November to 0300 UTC 21 November (the local experiment time is UTC − 8).

### b. Instrumentation

The *Sally Ride* provided observations of atmospheric conditions—air temperature, humidity, pressure, and precipitation, along with downwelling solar shortwave and longwave radiation. A flow-through CTD system recorded ocean temperature and salinity at 5-m depth. We also deployed a FastCTD system (Klymak et al. 2008), a winched CTD capable of profiling at speeds of 3–5 m $s^{-1}$, resulting in profiles to 200 m every 2–3 min.

Autonomous surface vehicles provide a rich dataset of atmospheric and near-surface observations. During the Catalina deployment, three Liquid Robotics SV2/SV3 wave gliders (*Planck*, *Stokes*, and *Kelvin*) were equipped with a meteorological package and flow-through CTD, a thermistor chain along the umbilical between 0- and 8-m depth, and an upward-looking Signature 1000 ADCP on the subsurface

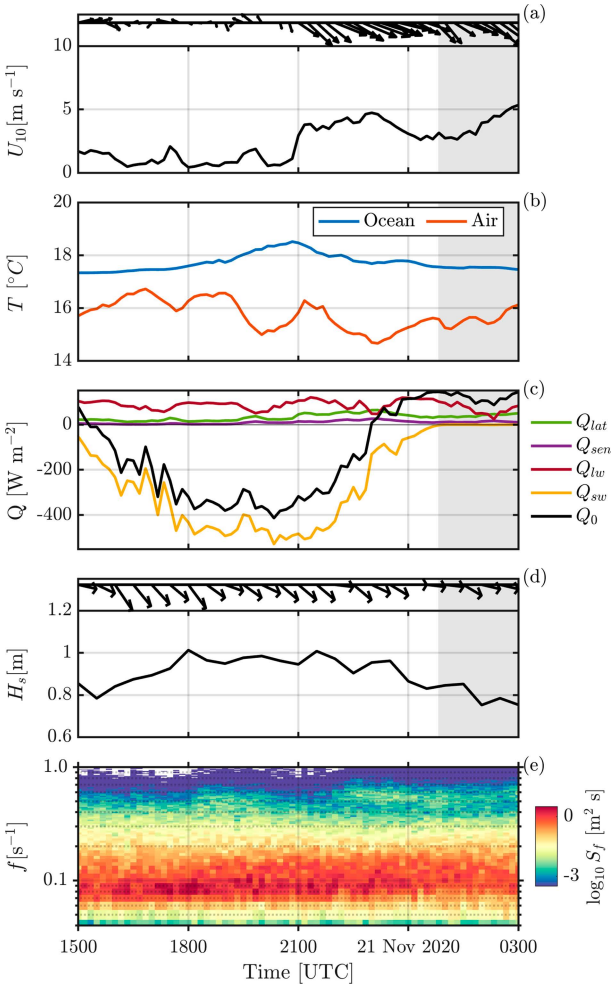


FIG. 2. Meteorological and oceanic forcing from wave glider *Planck*: (a) wind speed referenced to 10-m height $U_{10}$ with a feather plot indicating wind direction (going toward); (b) water temperature from CTD at 0.3-m depth (blue) and air temperature from wave glider met package at 1-m height (red); (c) surface heat flux components: latent heat (green), sensible heat (purple), net longwave radiation (red), downwelling shortwave radiation (yellow), and net surface heat flux (black), with positive values corresponding to ocean cooling; (d) significant wave height $H_s$ and wave direction at peak frequency (going toward); and (e) omnidirectional frequency spectrum of wave energy vs time, with the logarithmic color scale. Nighttime is shaded in gray.

platform and downward-looking ADCP mounted on the surface float (Grare et al. 2021; Hodges et al. 2023) (Fig. 3). The umbilical thermistor chains sampled at 1 Hz and provide a dense vertical resolution of temperature in the upper boundary layer, with thermistors at 0.70-, 0.95-, 1.20-, 1.45-, 1.80-, 2.30-, 2.80-, 3.55-, 4.30-, 5.05-, 6.05-, 7.05-, and 8.05-m depth, with an additional CTD mounted on the keel of the surface float at 0.31-m depth. The SV2 wave glider (*Kelvin*) has an additional thermistor chain extending to 40-m depth, enabling temperature observations through the base of the mixed layer which averaged about 25 m deep. The upward-looking ADCP provides high-resolution velocity measurements and backscatter

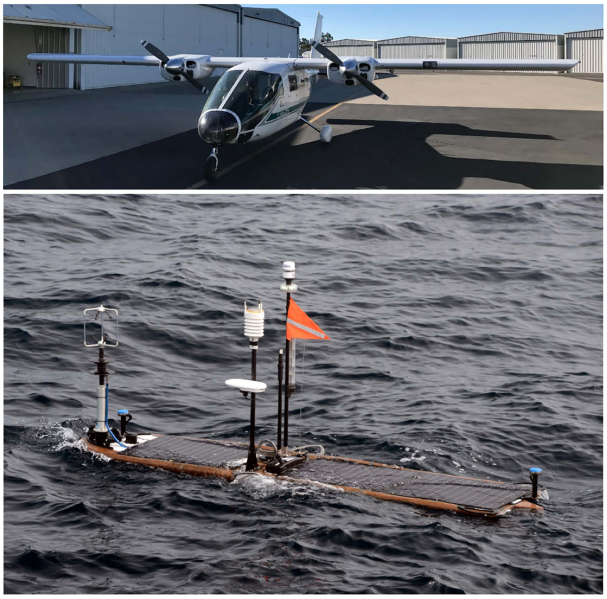

FIG. 3. (top) Research aircraft Partenavia P68 operated by Aspen Helicopters (Oxnard, CA), equipped with MASS, used for aerial surveys of the Catalina experiment region. (bottom) Surface platform and instrumentation of a deployed SV3 wave glider.

intensity from the vertical fifth beam at 2-cm resolution. The wave gliders also measure the directional wave field using high-precision GPS and inertial measurement units (IMUs) (Colosi et al. 2023).

During the Catalina deployment, airborne measurements were collected using the Modular Aerial Sensing System (MASS; Melville et al. 2016) during daytime low-altitude flights over the experiment region (Fig. 3). The primary instrument for this analysis is the longwave infrared camera in the 8.0–9.2-$\mu$m spectral range. The camera operates at 50 Hz and has a resolution of 0.5–2 m with a field of view from 300 to 1000 m, depending on flight altitude. Additionally, the MASS features a waveform scanning lidar to measure sea surface topography, which can be used as another record of directional wave information (Lenain and Melville 2017). The images collected by the aircraft are georeferenced using a 200-Hz GPS–IMU. One limitation to the airborne measurements is that collecting images of the sea surface required cloudless daytime conditions, which were rare during the deployment period in the Catalina basin. Composite images of SST are made by combining individual georeferenced images along the aircraft's flight path into a mosaic, with each 2 m $\times$ 2 m pixel formed by averaging about 900 images for a flight speed of 55 m s$^{-1}$, 50-Hz camera frequency, and 1000-m aperture. Temperature mosaics are examined individually, and only those with small background variability and no cloud contamination are used in the analysis. While infrared imaging of the sea surface has previously been used to calculate surface velocity using particle image velocimetry (e.g., Veron et al. 2008a; Vrećica et al. 2022), the transient flights here are incompatible with this technique as a given image area is not kept in frame for a sufficient time.

During both deployments, an array of drifting instruments supplemented temperature and velocity measurements with a greater depth range than the wave glider platforms alone. Five drifting Wirewalkers (Pinkel et al. 2011), vertically profiling wave-powered instruments, were deployed featuring a CTD and upward-looking ADCP (Zheng et al. 2022). Four of the instruments profiled to 500 m while the fifth went to 200 m. The profile repeat times vary with wave conditions, with the fastest repeats being every 7 min for the 200-m configuration during the largest swell and as long as every hour for the 500-m package in calm conditions. Two drifting thermistor chains (T-chains) were deployed with thermistor spacing every 2.5 m and an upward-looking ADCP at the bottom. One chain went to 100 m and featured additional dense thermistor spacing (0.5 m) in the thermocline, while the other chain went to 200 m. The sampling frequency of most thermistors was 2 Hz, with some up to 16 Hz.

### c. *Scale analysis*

To gauge whether LCs are expected to be an important OSBL driver during the selected observational period, we consider the relative importance of wave-driven turbulence to wind shear and convectively driven turbulence, following Li et al. (2005). The ratio of wind-forced to wave-forced TKE production is given by the turbulent Langmuir number $\mathrm{La}_t$ (McWilliams et al. 1997),

$$\frac{u_*^3/h}{w_{*L}^3/h} = \frac{u_*}{u_{s0}} = \mathrm{La}_t^2, \tag{1}$$

where $u_*$ is the friction velocity in water, $u_{s0}$ is the surface Stokes drift, and $h$ is the boundary layer depth. The friction velocity in water $u_*$ is calculated from the wind stress at the surface $\tau$ and the surface water density $\rho_0$ and is analogous to the friction velocity in air, $\rho_0 u_*^2 = |\boldsymbol{\tau}| = \rho_{\mathrm{air}} u_{*\mathrm{air}}^2$. The vertical velocity scale is given by $w_{*L} = (u_*^2 u_{s0})^{1/3}$ (Grant and Belcher 2009). In cases where the wind stress and Stokes drift are misaligned, a modified Langmuir number can be used (Van Roekel et al. 2012) since misalignment can impact the strength and orientation of LCs, as highlighted by recent numerical and observational studies (Wang et al. 2019; D. Wang and Kukulka 2021; X. Wang and Kukulka 2021; Wang et al. 2022). The LCs in this study are primarily driven by fetch-limited wind waves, which, especially at times of weak offshore wind, are misaligned with remote swell. The differentiation between wind waves and remote swell, along with a changing boundary layer depth, requires the use of a surface-layer Langmuir number (Harcourt and D'Asaro 2008). We follow Van Roekel et al. (2012) in using the surface-layer averaged and projected Langmuir number:

$$\mathrm{La}_{\mathrm{SL,proj}} = \sqrt{\frac{u_* \cos(\alpha)}{|\langle \mathbf{u}_s \rangle_{\mathrm{SL}}| \cos(\theta_{\mathrm{ww}} - \alpha)}}, \tag{2}$$

where $\langle \mathbf{u}_s \rangle_{\mathrm{SL}}$ is the depth average of the Stokes drift over the top 20% of the boundary layer, $\theta_{\mathrm{ww}}$ is the angle between the wind and the surface Stokes drift, and $\alpha$ is the angle between the wind and Langmuir cells, approximated by

$$\alpha \approx \tan^{-1}\left[\frac{\sin(\theta_{\mathrm{ww}})}{\frac{u_*}{u_{s0}\kappa}\ln(|h/z_1|) + \cos(\theta_{\mathrm{ww}})}\right], \tag{3}$$

with von Kármán constant $\kappa = 0.4$ and $z_1$ the onset depth of the law of the wall, approximated as four times the significant wave height $H_s$ (Li et al. 2016). We note that this scaling requires the mean Stokes drift shear over the surface layer to be approximated by the surface Stokes drift (Van Roekel et al. 2012). This assumption breaks down during periods of weak offshore wind forcing with a shallow diurnal warm layer, where the Stokes drift of short wind waves cancels the opposing swell contribution near the surface, dramatically reducing the Stokes drift shear within the surface layer, at times even inverting the sign of the Stokes drift shear. For the offshore region, the Stokes drift is assumed to be aligned with the wind, reducing (2) to $\mathrm{La}_{\mathrm{SL}}$.

We use a stability parameter $\Lambda$ (Chor et al. 2021) as a measure of the relative importance of convective turbulence to shear turbulence:

$$\Lambda = \kappa \frac{w_*^3}{u_*^3} = -\frac{h}{L_O}, \tag{4}$$

where $w_* = (B_0 h)^{1/3}$ is the turbulent convective velocity (Large et al. 1994) and $L_O$ is the Monin–Obukhov length, with surface buoyancy flux $B_0$. We choose to use $\Lambda$ as opposed to other commonly used scalings such as the Langmuir stability length (Belcher et al. 2012) or the Hoenikker number (Li et al. 2005) due to its recent use in studies of entertainment buoyancy flux in the surface boundary layer (Li et al. 2017; Chor et al. 2021; Pham et al. 2023). We note that Pearson et al. (2015) introduce a modified Langmuir stability length that uses an effective buoyancy flux to account for distributed radiative heating. While we could apply this modification to our buoyancy flux, we retain the surface definition here for simplicity.

Calculating the parameters $\mathrm{La}_{\mathrm{SL,proj}}$ and $\Lambda$ requires the water friction velocity $u_*$, surface buoyancy flux $B_0$, Stokes drift velocity $u_s$, and boundary layer depth $h$. $u_*$ and $B_0$ are obtained with the help of the COARE algorithm for calculating air–sea fluxes (Fairall et al. 2003), using inputs of observed ocean-relative wind speed, air temperature, pressure, humidity, precipitation, radiative fluxes, near-surface ocean temperature, and significant wave height and phase speed. Atmospheric and ocean measurements from wave glider *Planck* were supplemented with downwelling solar radiation measurements from the *Sally Ride*. The friction velocity in water $u_*$ is calculated from $\boldsymbol{\tau}$, and the sea surface density $\rho_0$ is calculated from the wave glider CTD at 0.31-m depth. Surface buoyancy flux is given by

$$B_0 = -\frac{g\alpha}{\rho_0 c_p} Q_0 + g\beta(E - P)S_0, \tag{5}$$

where $\alpha$ and $\beta$ are thermal expansion and haline contraction coefficients, respectively; $c_p$ is the specific heat of water; $Q_0$ is the net surface heat flux, combined from incoming shortwave

solar radiation, net longwave radiation, latent, and sensible heat fluxes (Fig. 2c); and $E - P$ is the freshwater flux (m s$^{-1}$) (Cronin and Sprintall 2009), with $S_0$ the surface salinity. There was no precipitation during the experiment, and stratification is set by temperature. Negative $B_0$ corresponds to stabilizing surface forcing (warming).

The boundary layer depth $h$ is commonly defined as the region with active turbulent transport (Li et al. 2016) and can differ substantially from both the depth of the mixed diurnal warm layer and the deeper seasonal mixed layer (Pearson et al. 2015). For scaling in the Catalina basin, we define the boundary layer depth as the depth of the maximum vertical temperature gradient, within the depth range observed by the wave glider thermistor chain (0.31–8.05 m). Alternative boundary layer definitions are explored in section 4. A 2-h moving mean is applied to $h$ for use in this scale analysis. The mixed layer depth in the Catalina basin was about 25 m, as determined by a density difference relative to the 10-m density equivalent to a 0.2-K temperature difference, following de Boyer Montégut et al. (2004). For the offshore experiment, in the absence of an observable diurnal warm layer, the boundary layer depth is taken to be equivalent to the mixed layer depth.

To characterize observations of Langmuir circulations, the Stokes drift $\mathbf{u}_s$ is calculated from observations of the directional wave spectra from wave gliders. The leading-order expression for the full Stokes drift of a spectrum of deep-water waves (Kenyon 1969; Webb and Fox-Kemper 2011) is given by

$$\mathbf{u}_s = \frac{16\pi^3}{g}\int\int(\cos\theta,\ \sin\theta,\ 0)f^3S(f,\ \theta)e^{(8\pi^2f^2z)/g}\,d\theta\,df. \tag{6}$$

Directional wave spectra $S(f,\ \theta)$ were estimated from the motion of the wave gliders (Colosi et al. 2023). While the low-frequency swell waves are more energetic, high-frequency wind waves contribute more to the Stokes drift and its gradient near the surface due to their increased steepness and rapid decay with depth. Wave gliders are capable of resolving frequencies of up to about 1 Hz. In fully developed seas, the directional spectra can be extended with a tail to account for the Stokes drift contribution from unresolved frequencies (Belcher et al. 2012; Lenain and Pizzo 2020). A tail with an $f^{-4}$ slope is fit up to wavenumber $k_n = rg/u_{*\mathrm{air}}^2$, the predicted transition between the equilibrium and saturation ranges, with $r = 9.7 \times 10^{-3}$. For wavenumbers above $k_n$, an $f^{-5}$ slope is fit out to a cutoff wavenumber $k_M$ above which the directional spectrum is assumed to be isotropic, resulting in zero Stokes drift, with $k_M = (g/u_{*\mathrm{air}}^2)e^{(\pi/2-\theta_0)/\gamma}$, $\theta_0 = 2.835$, and $\gamma = 0.48$, following Lenain and Melville (2017). The wave spectra were computed in 10-min segments and were rescaled to preserve variance relative to the wave glider heave time series. A limitation of this methodology is the inability to resolve the Stokes drift contribution from small wind waves that were above 1 Hz (shorter than $\lambda \approx 1.6$ m). In wind–wave equilibrium, the contribution of unresolved waves to the total surface Stokes drift is about 15% although the relative importance decays rapidly with depth (Lenain and Pizzo 2020). For a fetch-limited breeze in the absence of swell, the unresolved Stokes drift contribution is much larger.

As an attempt to correct for unresolved wind waves, the Stokes drift was also calculated from a wind-based parameterization of the wave spectrum. Pizzo et al. (2019) (hereafter, P19) give the surface Stokes drift $u_{s0}$ based on parameterization of the wave spectrum for equilibrium and saturation ranges developed in Lenain and Melville (2017). While estimates of the depth profile of Stokes drift based on the surface magnitude, such as the Phillips spectrum profile, are commonly used (Breivik et al. 2016; Breivik and Christensen 2020), we instead extend the surface Stokes drift approximation in P19 Eq. (11) to arbitrary depth by adding an exponential decay with depth inside the integral, giving

$$u_s(z) = 1.6\int\phi(k)\sqrt{gk}ke^{2kz}\,dk, \tag{7}$$

with the wave spectrum given by

$$\phi(k) = \begin{cases} \phi_E(k) = \dfrac{1}{2}\beta u_{*\mathrm{air}}g^{-1/2}k^{-5/2} & k \in (k_p,\ k_n), \\ \phi_S(k) = Bk^{-3} & k \in (k_n,\ k_M), \\ 0 & \text{otherwise}, \end{cases} \tag{8}$$

where $k_p$ is the peak wave frequency, determined from the wave glider observations, while the parameters $\beta$, a constant scaling for the equilibrium range, also called Toba's constant, and $B$, the saturation constant, are empirically determined by Lenain and Melville (2017) to be 0.08 and $7 \times 10^{-3}$ rad, respectively. The contribution of low wavenumbers $k < k_p$ is ignored following Breivik et al. (2014) since the wave slopes are small, as is the contribution above the high-frequency cutoff $k > k_M$. The Stokes drift magnitude calculated from this omnidirectional spectrum is reduced by 20% relative to a monochromatic wave to account for wave spreading (Webb and Fox-Kemper 2015). Our best estimate of the in situ Stokes drift is constructed by adding the Stokes drift from the observed directional wave spectrum, integrated up to the wave glider resolution limit of 1 Hz, with a wind wave Stokes drift from the P19 parameterized spectrum, integrated between 1 Hz and the isotropic high-frequency cutoff $k_M$.

For computational efficiency in the LES run, the Stokes drift is prescribed entirely from the parameterized wave spectrum. To better match the observed wave spectra in fetch-limited winds across the full frequency range, we rescale the parameterization constants to $\beta = 0.048$ and $B = 2.4 \times 10^{-3}$, as a given wind friction predicts too much low-frequency energy and much of the wind energy input goes into growing surface waves rather than breaking-driven dissipation. Furthermore, $k_p$ is set to a constant $k_p = 0.036 = 2\pi/173$ m to simplify inputs to the LES run. We assume the wave direction to be the same as the wind direction, removing any misalignment effects between wind waves and the remote swell in the LES.

Figure 4 compares the Stokes drift calculated from 1) the uncorrected omnidirectional spectrum from wave glider

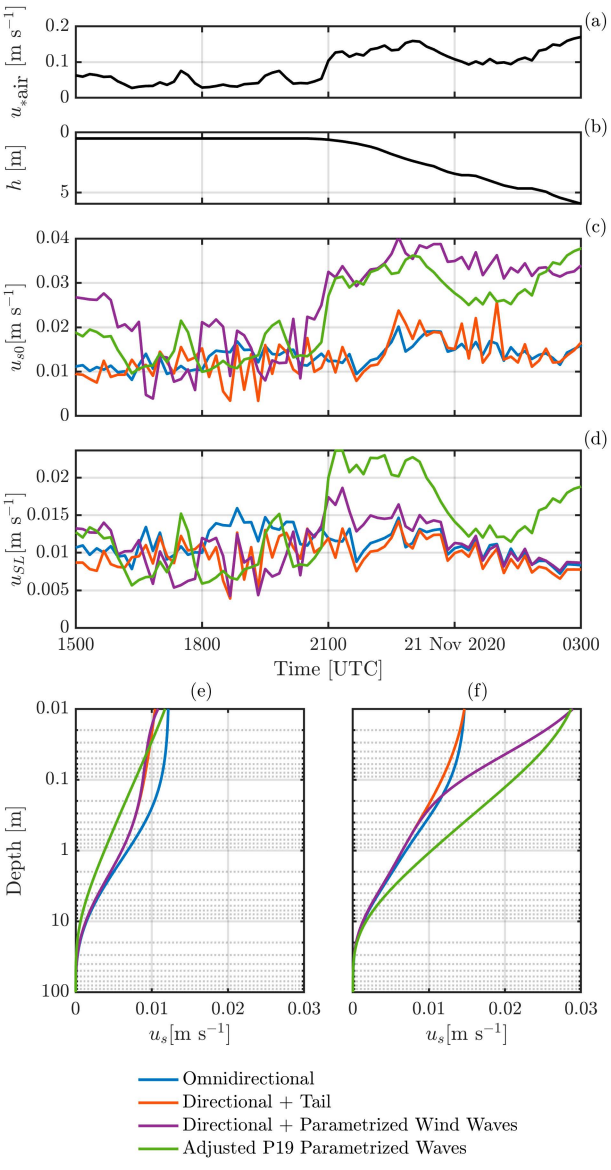


FIG. 4. Time series of (a) wind friction velocity in air $u_{*air}$, (b) boundary layer depth $h$, (c) Stokes drift at the surface, and (d) the surface-layer average Stokes drift. Stokes drift profiles averaged over (e) the low-wind period from 1500 to 2030 UTC 20 Nov 2020 and (f) the high-wind period from 2130 UTC 20 Nov to 0300 UTC 21 Nov 2020. Stokes drift is computed from the observed omnidirectional wave spectrum (blue), the observed directional wave spectrum with added high-frequency tail (red), the observed directional wave spectrum with wind waves from the P19 parameterization, used to compute the Langmuir number in Fig. 5 (purple), and the tuned P19 wind-based parameterization used in the LES run (green).

observations, 2) the observed directional spectrum with a tail correction out to isotropic wavenumbers, 3) the observed directional spectrum with additional wind waves above 1 Hz from the P19 wind-based parameterization, and 4) the adjusted P19 parameterized wave spectrum, used for the LES run. The average Stokes drift profiles for the observation period agree well, with the wind parameterizations larger than observation near the surface due to the added wind wave contribution. During low wind conditions, the surface Stokes drift $u_{s0}$ time series agree, but the wind-based parameterizations respond more rapidly to the changing wind forcing. At around 2130 UTC, the addition of parameterized wind waves to the observed waves results in a 3× larger surface Stokes drift versus direct observations.

Phase diagrams characterizing the relative importance of wind, wave, and buoyancy forcing have been constructed by Li et al. (2005), Belcher et al. (2012), and Li et al. (2019), who find that open-ocean fully developed sea states typically correspond to a wave-driven upper ocean with $La_t \approx 0.3$. To contextualize our study, we plot the distribution of observations in the $La_{SL,proj}$ versus $\Lambda$ parameter space (Fig. 5) following Chor et al. (2021). In the Catalina experiment, on 20 November, the buoyancy flux is strongly stabilizing until about 1830 UTC when the wind increases at the location of the wave glider. At about 2315 UTC, the buoyancy stability changes sign to convectively cooling ($\Lambda > 0$) but does not dominate over Langmuir turbulence. During the offshore experiment, wind and wave forcing was much greater.

An alternative to regime diagrams is constructed by Gargett (2022) using the surface buoyancy flux and LC growth rate $g_*$:

$$g_* = \left[\left\langle \frac{du_s}{dz} \right\rangle_{SL} \frac{u_*}{h}\right]^{1/2}, \tag{9}$$

where we have chosen to use the surface-layer average Stokes drift shear (from 0 to $0.2h$) rather than the shear at a fixed depth (Gargett and Grosch 2014). The forcing space highlights the peak in the combined wind and wave forcing in the Catalina experiments coincident with the onset of the sea breeze (Fig. 5c). Indeed, as we see later, this peak is coincident with the fastest deepening of the diurnal warm layer. In the offshore region, the LC growth rate is largest at the wind peak when we observe mixed layer deepening. Despite the stronger wind and wave forcing, the LC growth rate was smaller than in the Catalina basin because of the deeper boundary layer and the larger relative contribution of longer waves, which reduced the Stokes drift shear. We understand the regime diagrams and forcing space diagrams to be complimentary. While the regime diagrams are useful in understanding the dominant contribution to turbulent processes, the forcing space diagrams are more predictive of the effect of forcing one expects to observe.

### d. *Large-eddy simulation*

A large body of work uses large-eddy simulations to study Langmuir turbulence (Skyllingstad and Denbo 1995; McWilliams et al. 1997; Skyllingstad et al. 2000; Tejada-Martínez and Grosch 2007; Kukulka et al. 2009; Van Roekel et al. 2012; Sullivan and McWilliams 2017; D. Wang and Kukulka 2021). LES is a model that resolves motions of a low-pass spatial filter of the Navier–Stokes equations while parameterizing small-scale turbulence motions (Smagorinsky 1963; Deardorff 1970; Moeng 1984). In the case of LES for LT, the equations are temporally averaged

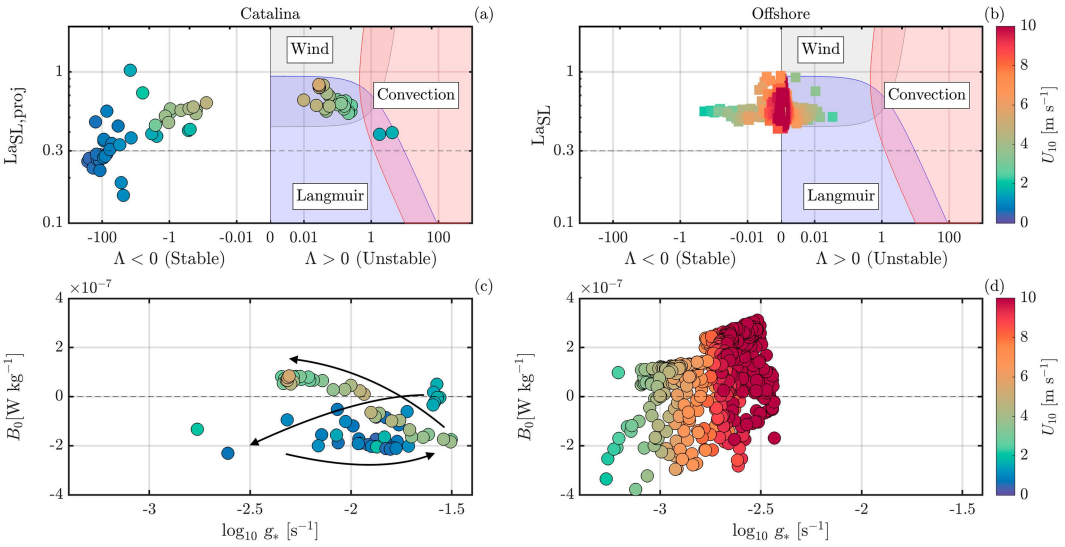


FIG. 5. Scale analysis of the forcing in (left) the Catalina basin and (right) the offshore experiment, shown as a scatterplot of 10-min binned observations, colored by the 10-m wind speed. (a),(b) The nondimensional parameter space $La_{SL,proj}$ vs $\Lambda$. The $x$ axis is divided into regions of stable buoyancy forcing on the left ($\Lambda < 0$) and unstable convective forcing on the right ($\Lambda > 0$). For unstable buoyancy forcing, colored regions show where a forcing mechanism contributes at least 25% of TKE production, for wind (gray), wave (blue), and convective (red) forcing for the parameter space $La_t$ vs $\Lambda$. The dashed line traces the wind–wave equilibrium at $La_t = 0.3$. These characterizations of the parameter space have not been rescaled to account for the difference between using the surface value of Stokes drift instead of the surface-layer average. The plot is logarithmic except in the region $|\Lambda| < 0.01$, where the $x$ axis is linear. (c),(d) Forcing parameter space $B_0$ vs $g_*$. Arrows in (c) indicate the time progression of forcing, from morning wind bursts, to stabilizing heating with low winds, to the onset of wind, and the transition to nighttime convection. The time series of the forcings is provided in appendix B (Fig. B1).

over irrotational surface gravity waves and include a CL vortex force (McWilliams et al. 1997). Simulations can be either idealized, to study specific physical processes, or forced with realistic conditions, to study the real-world behavior of LT and compare with observations (Kukulka et al. 2009; Fan et al. 2020).

The LES setup used here is based on the NCAR model used in Sullivan et al. (2012). Lateral boundaries are periodic, with prescribed momentum and density fluxes at the surface and outward wave radiation with zero stress at the bottom. Unresolved subgrid-scale motions (SGSs) are parameterized following Deardorff (1970) and Sullivan et al. (2007). The domain size is 300 m × 300 m × 50 m, with 1024 × 1024 horizontal grid cells and 128 vertical levels, giving lateral spacing $\Delta x = \Delta y = 0.29$ m and varying vertical spacing from $\Delta z = 0.08$ m at the surface to 1.12 m at the bottom, with the top grid cell at 0.0375-m depth and the bottom grid cell at 49.435-m depth. The model may be underresolved for the Stokes drift shear from the shortest wind waves, which have centimeter-scale $e$-folding depth. The model uses an adaptive time-stepping scheme with a time step chosen to maintain the CFL condition, which ranged from a maximum of about 4 s to a minimum of around 1 s for the more energetic periods.

The LES model requires a subgrid-scale parameterization for turbulent length scales smaller than the mixing length $l$. The mixing length depends on the grid spacing and the stability of the boundary layer. For an unstable or neutral boundary layer, then $l$ is simply a measure of the mean grid spacing:

$$l_{\text{unstable}} = \Delta = (\Delta x \Delta y \Delta z)^{1/3}. \tag{10}$$

For a *stable* boundary layers, however,

$$l_{\text{stable}} = 0.76 \frac{e^{1/2}}{N}, \tag{11}$$

which depends upon the Brunt–Väisälä frequency $N$ and the SGS turbulent kinetic energy $e$. To capture turbulence scales below the filter scale $l$, the evolution of the SGS turbulent kinetic energy is given by an advection–diffusion equation:

$$\partial_t e + (\mathbf{u} + \mathbf{u}_s) \cdot \nabla e = S_s + S_b + S_d - \epsilon, \tag{12}$$

where $S_s$ is the shear production of turbulence, $S_b$ is the buoyancy production, $S_d = \nabla \cdot (\nu_m \nabla e)$ is the TKE diffusion, and $\epsilon$ is the viscous dissipation (Sullivan et al. 2016). To close the evolution equation for $e$, the dissipation $\epsilon$ needs to be parameterized in terms of $e$ and the mixing length. This is modeled as

$$\epsilon = \left(0.19 + 0.5 \frac{l}{\Delta}\right) \frac{e^{3/2}}{l}. \tag{13}$$

Two LES model runs are presented here: an idealized run, to study the onset of LCs in section 3, and a realistic run forced from observations, to study the growth of LCs during boundary layer deepening in section 4. The initialization and forcing of the runs are detailed in their respective sections. In both runs, wave forcing is included through a parameterized Stokes

drift profile based on the observed wind friction (Fig. 4). Radiative heating in the model is only applied at the top grid cell. The sensitivity of the model response to radiative heating and attempts to correct those effects are described in later sections. In brief, confining heat flux to the top grid cell results in higher temperature and stratification than observations. A better parameterization for the radiative forcing (see Pham et al. 2023) is needed to address the significant sensitivity in the LES model presented here, but its implementation is beyond the scope of this work.

## 3. Onset of Langmuir circulations

### a. *Fetch-limited wind forcing*

On the morning of 20 November 2020, between 1700 and 1800 UTC (0900–1000 LT), aircraft transects were performed over the experiment region (Fig. 6a). Wind speed along the flight track is determined from mean-square wave slope observations (Lenain et al. 2019). The plotted wind direction along the flight track is computed spectrally from the orientation of the observed Langmuir cells in the infrared imagery, where they are present. On the eastern side of the experiment region, winds were up to 3 m $s^{-1}$ toward the southwest. Further west, wind speeds decreased to less than 1 m $s^{-1}$ and rotated toward the west. The wind pattern is indicative of a weak land breeze that was partially blocked by Catalina Island, forming a wind shadow over the experiment region.

### b. *Airborne infrared observations*

Sea surface temperature was collected in transects across the experiment region using an airborne infrared camera (Fig. 7). In areas of low wind speeds (<1 m $s^{-1}$), the sea surface exhibited large-scale incoherent convective patterns (Figs. 8a,b) broadly attributable to surface renewal processes (Gargett et al. 2004). In regions of moderate winds of 1–2 m $s^{-1}$, Langmuir cells started to appear (Fig. 8c). Narrow bands associated with convergent and downwelling regions are colder than the broader upwelling areas. This pattern is attributed to the convergence and thickening of the surface cool skin above the downwelling sites, while warmer water from the shallow warm layer is upwelled to areas of surface divergence, resulting in a thinner and thus relatively warmer skin temperature (Marmorino et al. 2005). The cells first appear in patches of about 50 m in diameter, interspersed between areas of uniformly colder surface temperature (Figs. 7b–d). Within patches of LCs, temperature streaks have a cross-cell spacing of about 2 m (Fig. 8d). In regions of winds at 3 m $s^{-1}$, the cells become more organized and uniform, with few patches of interruption, and are spaced by about 5 m (Figs. 8e,f).

#### 1) Spatial inhomogeneity of LC onset

For initial wind forcing, the surface signature of LCs appears nonuniformly. A close-up of one composite IR frame (Fig. 9) highlights the sharp contrast between a cold patch of unbroken cool skin and streaked temperature signatures of LCs around it, with an especially sharp contrast on the downwind side of the cold patch.

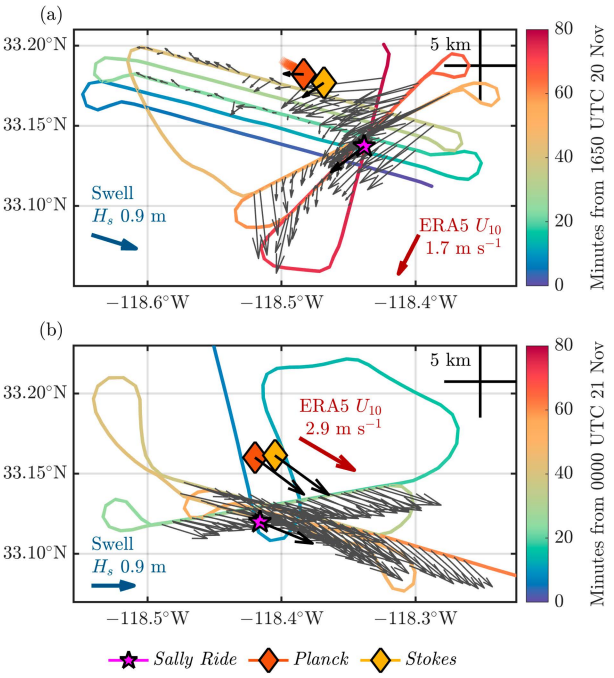


FIG. 6. Flight track of aircraft transects and positions of assets with wind vectors for (a) the morning flight during a weak land breeze and (b) the afternoon flight during a stronger sea breeze. The width of the flight track shows the area imaged by the IR camera and is to scale geographically. Arrows indicate wind velocity. Light gray arrows are the 10-m wind magnitude derived from the mean-square wave slope using airborne lidar, with wind direction reconstructed from the orientation of Langmuir cells, where they are present. Bold black vectors are 10-m winds derived from direct observations of wind speed from meteorological instruments on the wave gliders and *Sally Ride*. The red arrow is the ERA5 reanalysis 10-m wind, interpolated to the center point of the experiment region. The blue arrow indicates the peak wave direction.

Thermal signatures of surface gravity waves with about 10-m wavelengths can be seen within the cold patch. The temperature signal of surface waves is likely due to mechanical straining of the surface (Veron et al. 2008b). Rapid distortion theory (Teixeira and Belcher 2002) predicts that for a sufficiently weak surface turbulence field, orbital wave motions can become the dominant surface strain signal, stretching and contracting the surface skin. Stretching of the cool skin in wave troughs would result in positive temperature anomalies as slightly warmer cool skin water comes to the surface. In areas where LCs have developed, turbulence is higher, obscuring the surface wave temperature signal. These may be the first ocean observations showing the contrast between two regimes of surface straining.

The dampening of turbulence and signature of relatively long surface waves in regions of unbroken cool skin layers is suggestive of the theory by Longuet-Higgins (1996) describing the exclusion of shorter wavelength surface waves in regions of convergence and downwelling. If large-scale incoherent temperature structures seen at low wind speeds (Fig. 7a) correspond to convective patterns, with convergent regions

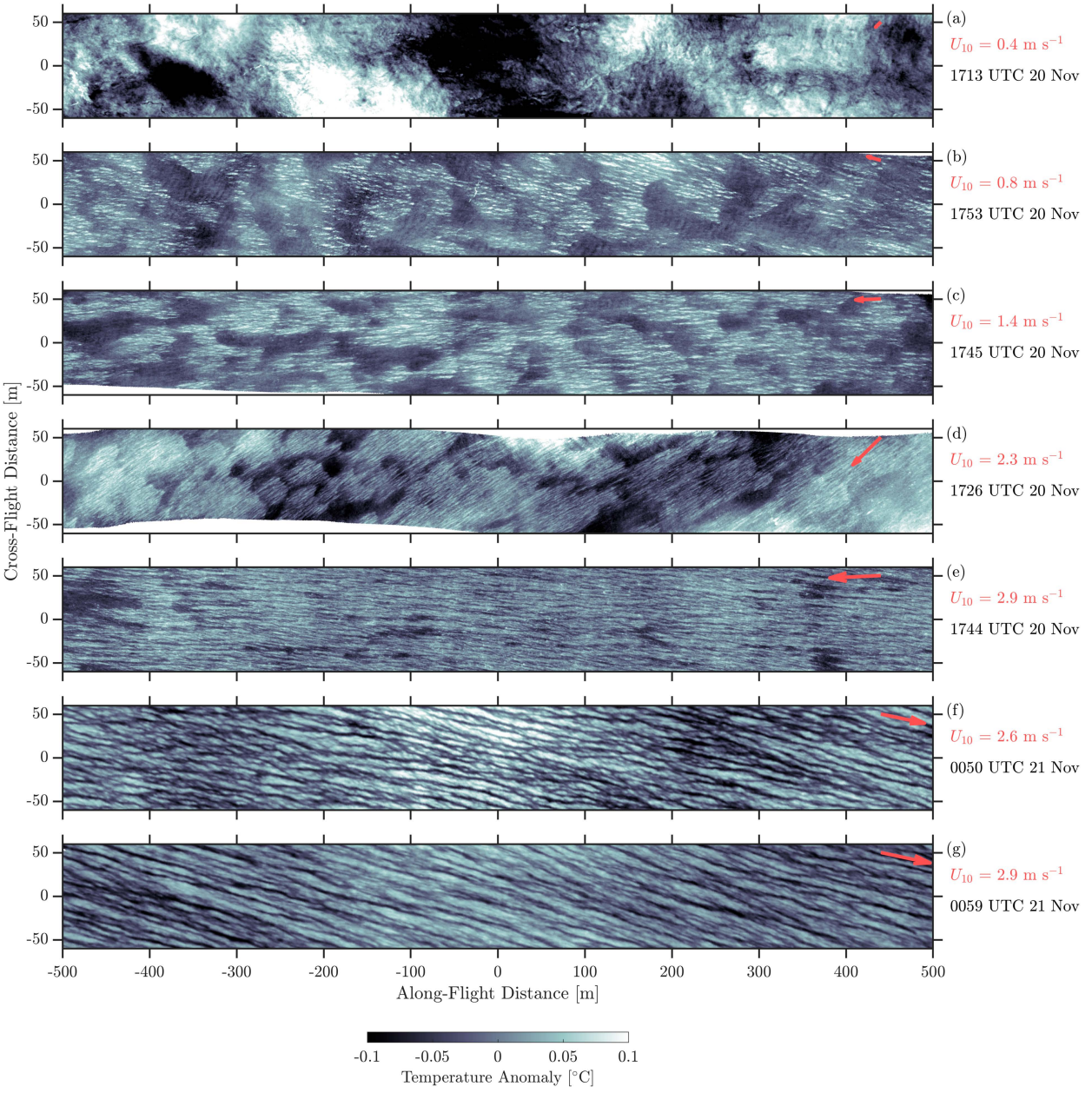


FIG. 7. Surface temperature from transects of airborne IR imagery. (a) Before the onset of wind, temperature is characterized by large-scale structures and convective turbulence. (b)–(d) The onset of wind forcing leads to the appearance of LCs, interspersed with unbroken patches of colder surface skin. (e) Under stronger wind forcing, cold patches disappear, and the LC field homogenizes. (f),(g) After several hours of sustained wind forcing and mixed layer deepening, LCs have formed larger, coherent streaks. The temperature anomaly is relative to the 2D plane fit of temperature to each panel, to remove background variations in temperature across the survey region. Areas of surface convergence and downwelling appear as negative temperature anomalies due to the convergence and thickening of the cool skin layer (Marmorino et al. 2005). Red arrows indicate wind magnitude, determined from the mean-square wave slope in each panel (Lenain et al. 2019), with flight-mean directions −150° in (a)–(e) and −28° in (f) and (g) obtained from nearby wave glider observations.

having colder, thicker cool skin, then shorter and steeper wind waves, responsible for the onset of LCs, may be excluded from the colder convergent regions. The stronger near-surface Stokes drift of shorter waves would drive LCs to first appear away from cold patches. This pattern of LCs at their onset is also reminiscent of laboratory experiments by Veron and Melville (2001) showing larger wave slopes in regions of warmer temperature at the onset of LCs. A conceptual schematic of our understanding of this process is shown in Fig. 10. Note that these observations occur during a period of stabilizing surface buoyancy flux, so conventional depth scaling for possible convective patterns does not apply. We

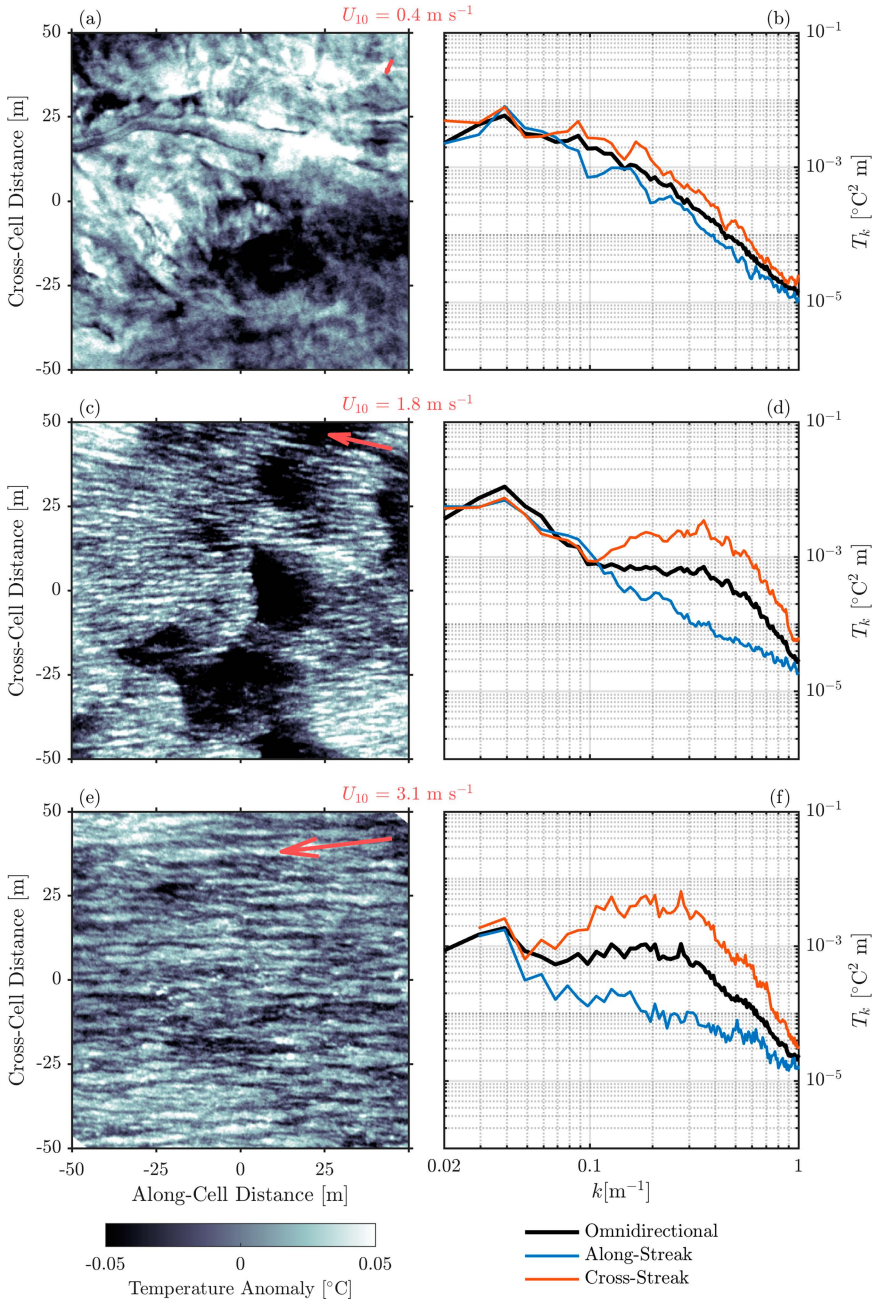


FIG. 8. Representative samples of surface temperature from the airborne IR camera for (a) low winds with no LCs, (c) the onset of LCs, and (e) organized LCs at moderate wind speeds. (b),(d),(f) The associated temperature wavenumber spectra compare the omnidirectional (black) spectrum with the cross-cell (red) and along-cell (blue) components. Temperature anomaly is relative to the 2D plane fit of temperature in each panel. Red arrows indicate wind magnitude, determined from the mean-square wave slope in each panel (Lenain et al. 2019), with flight-mean direction −150° obtained from nearby wave glider observations.

hypothesize that a mechanism for near-surface convective patterns during daytime heating comes from the balance between heat loss at the surface from latent cooling heat flux and outgoing longwave radiation with more distributed heating from incident shortwave radiation. For typical daytime values of surface heat loss (100 W m$^{-2}$) and shortwave radiation (500 W m$^{-2}$), the net buoyancy flux, computed from the double exponential irradiance model of Paulson and Simpson (1977), is destabilizing to $\mathcal{O}(0.1)$ m depths, which would suggest the formation of near-surface convection to those depths.

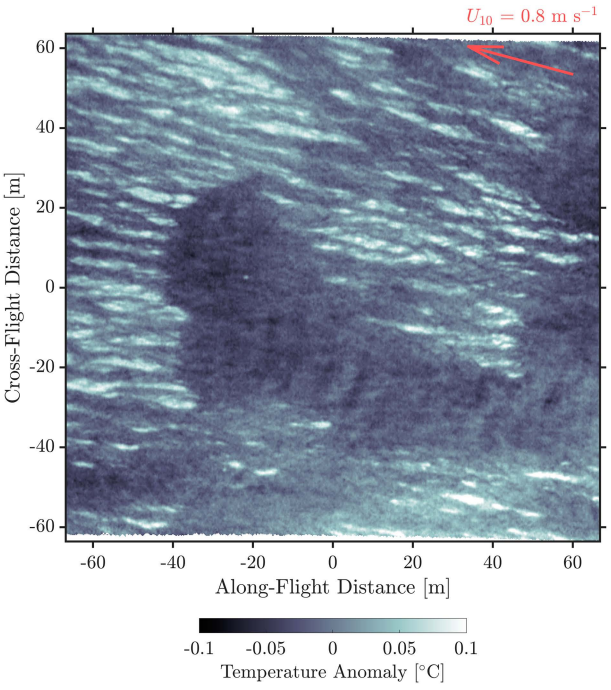


FIG. 9. Composite IR camera frame showing the sharp contrast between regions with LCs and a patch of unbroken cool skin. Wind (red arrow) is oriented toward the top left, with magnitude derived from mean-square slope and flight-mean direction −150° obtained from nearby wave glider observations. The signature of surface waves with about 10-m wavelength oriented in the direction of the wind can be seen in the cold patch. Temperature anomaly is relative to the 2D plane fit of temperature.

The Stokes drift $e$-folding depth $\delta = \lambda/(4\pi)$ of short $\mathcal{O}(\lambda = 1)$ m wind waves is similarly $\mathcal{O}(0.1)$ m, which would suggest the ability of this near-surface convection to influence the waves. Other processes that might lead to the inhomogeneous appearance of LCs include atmospheric turbulence that creates variability in the wind field or surface buoyancy flux and the clumping of surfactants in convergence regions, causing dampening of very short waves. The patchy appearance of LCs warrants further study of the coupled feedback between wave-forced turbulent instability and the wave field (Wagner et al. 2023).

#### 2) SEA SURFACE TEMPERATURE WAVENUMBER SPECTRA

To quantify the evolution of LC scales, temperature wavenumber spectra are constructed for the composite images (detailed in appendix A). The temperature spectra are separated into their cross-cell and along-cell components (Figs. 8b,d,f). This spectral procedure is repeated over 733 independent square segments of IR images, and the resulting spectra are binned by wind speed (Fig. 11). At low wind speed, before the appearance of LCs, the temperature wavenumber spectrum is isotropic and closely follows a $k^{-2}$ slope. As winds increase, temperature variance is enhanced in the crosswind direction, starting at 2-m scales and growing to 5-m scales. As the peak of the crosswind variance grows, we see a simultaneous decrease in along-wind variance. We interpret this spectral signature as the stretching of temperature features in the along-wind direction, emphasizing gradients in the crosswind direction. At 5-m scales, this redistribution of spectral power results in a 7× increase in crosswind power and a 3× decrease in along-wind power over the growth from 0 to 3.5 m s$^{-1}$ winds.

### c. *Comparison with idealized LES*

The observed dependence of temperature spectra on wind speed is compared with the appearance of LCs in an idealized LES run (Fig. 12). The idealized run is initialized with zero velocity and uniform 17.3°C temperature and forced with a constant 90 W m$^{-2}$ heat flux at the top grid cell, representative of the heating leading up to the morning observations. Wind forcing is ramped using a tanh function from 0 to 3.5 m s$^{-1}$ over the course of an hour. An attempt was made to use distributed shortwave forcing (Paulson and Simpson 1977), which resulted in a deeper initial boundary layer with reduced stratification, but this configuration did not show the appearance of LCs during wind forcing. We attribute this to overly active convective instability in the model, which is introduced by the surface cool skin.

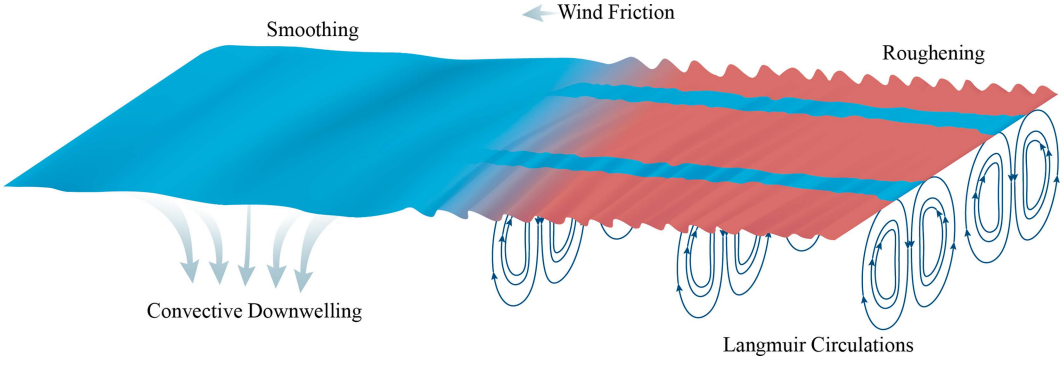


FIG. 10. Conceptual schematic showing the spatial filtering effect of a convective downwelling region on surface gravity waves, leading to a suppression of high-wavenumber waves within the convective region and enhancing high-wavenumber energy outside the patch. The higher near-surface Stokes drift outside of the downwelling region leads to earlier onset of LCs.

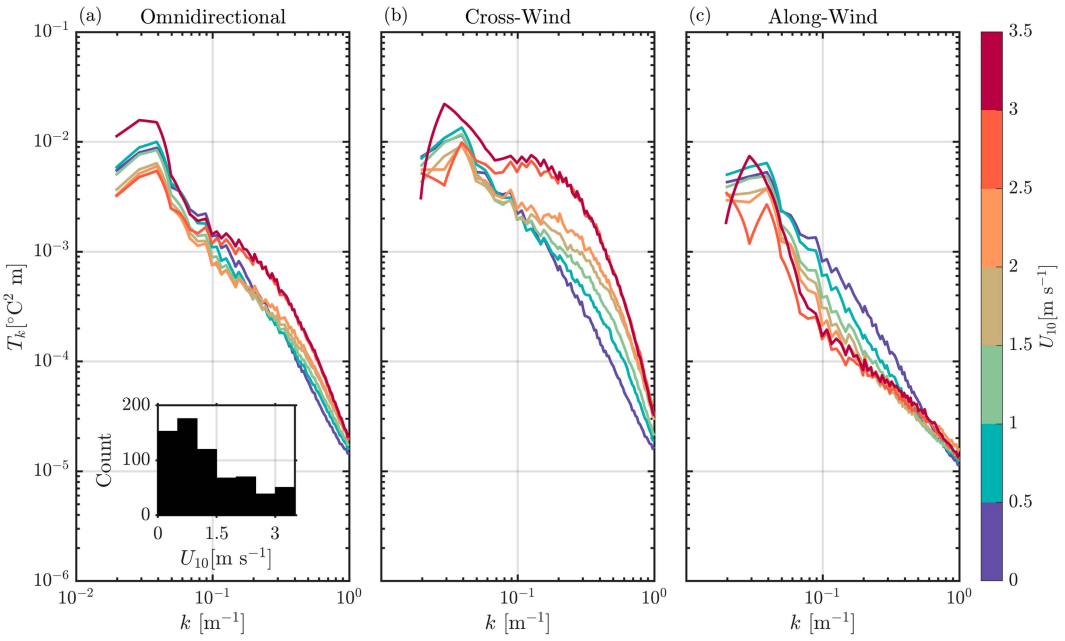


FIG. 11. Spectra of observed sea surface temperature in the (a) omnidirectional, (b) crosswind, and (c) along-wind directions, binned by wind speed. The inset shows a histogram with the number of spectra in each wind bin.

Figure 13 shows $x$–$y$ snapshots of temperature in the top grid cell and the associated horizontal spectra of temperature, analogous to the observations in Fig. 8. Note that that the color map for LES temperature is inverted; since the LES does not have cool skin, we expect divergent upwelling regions to have negative temperature anomalies and convergent downwelling regions to have positive temperature anomalies. At low wind speeds, the model shows random temperature fluctuations associated with incoherent turbulence. Organized streaks associated with LCs first appear in the LES at larger wind speeds than in observations, and they appear at much smaller scales, likely due to the shallower warm layer. We attribute the increase in cross-streak temperature variance and decrease in along-streak variance at 1-m length scales in Fig. 13d to early LCs. The peak in the cross-cell spacing at this early stage in their evolution may be at scales smaller than 1 m that are poorly resolved. As the wind continues to ramp, the peak in the crosswind spectra shifts to a lower wavenumber, as in the observations (cf. Fig. 8f with Fig. 13f). Coherent streaks are visible in the surface temperature of Fig. 13e, but their along-wind coherence appears to be shorter than in observations. In upwelling (cold) regions, temperature patterns appear to more strongly resemble convection, possibly associated with overly active model convection.

## 4. Growth of Langmuir circulations and diurnal warm layer deepening

### a. *Afternoon sea breeze*

Following the morning land breeze, winds decreased and generally remained under 1 m s$^{-1}$ during the day, while solar heating continued to stratify the shallow diurnal warm layer. On the afternoon of 20 November 2020, a northwesterly sea breeze ramped wind speeds from 1 to 4 m s$^{-1}$ over 15 min, after which winds remained at a consistent 2–3 m s$^{-1}$ for several hours into the evening. The wind direction was toward the southeast through the channel, aligned in the same direction as the swell (Fig. 6b).

Over the duration of these sustained winds, the diurnal warm layer was observed to deepen from 1 to 5 m (Fig. 14). To quantify the deepening rate, we compute two measures of the DWL depth (DWLD). One estimate is based on the depth of the maximum stratification $H_N$ computed from the temperature gradient on the wave glider T-chain. The deepening rate from 2100 to 0200 UTC, as determined by the depth of the maximum stratification, averaged 1 m h$^{-1}$ (Fig. 18). Our ability to quantify the strength and depth of the DWL is limited by the vertical spacing of temperature measurements. The CTD on the wave glider surface platform recorded temperature at 0.31-m depth, while the shallowest thermistor on the wave glider T-chain was installed at 0.70 m relative to the surface, meaning that DWLD shallower than 0.7 m could not be resolved. Until the onset of wind, the maximum stratification was recorded between the CTD and the shallowest thermistor, reaching a maximum value of 40 h$^{-1}$. Another estimate of DWLD is defined by the potential energy anomaly $H_\phi$ following Reichl et al. (2022) and Wang et al. (2023). To emphasize the shallow warm layer depth, we choose $\phi = 0.3$ J m$^{-1}$, which matches the two depth estimates toward the end of the observations but results in an overestimate of DWLD for $H_N < 2$ m.

### b. *Airborne infrared and subsurface observations*

After 3 h of sustained winds at 3 m s$^{-1}$, an aircraft flight from 0000 to 0100 UTC 21 November observed coherent

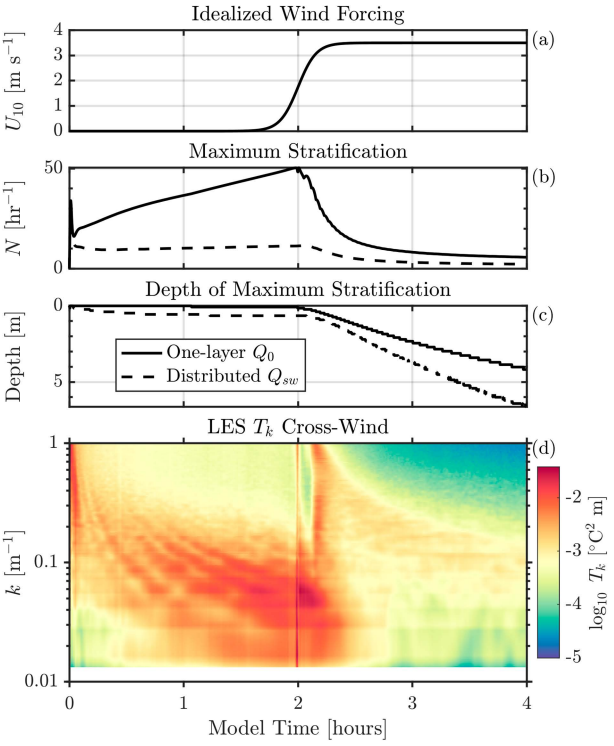


FIG. 12. (a) Idealized wind ramp from 0 to 3.5 m s$^{-1}$ used in the idealized LES run. (b) Maximum stratification and (c) the depth of the stratification maximum from the one-layer heat flux model (solid) and distributed shortwave model (dashed). (d) Crosswind spectra of temperature from the surface grid cell from the one-layer heat flux run. The sharp variance peak at 2 h into the run is attributed to insufficient vertical resolution during the most highly stratified time window.

Langmuir circulations throughout the experiment region (Figs. 7f,g). Cross-cell scales were about 15 m throughout the experiment region (Figs. 15a,b), roughly 2.5 times the depth of the shallow warm layer at that time, whose maximum stratification had decayed to 10 h$^{-1}$ (Fig. 18).

The T-chain on the wave gliders can provide a subsurface view of lateral and vertical LC scales. To convert time from the thermistor record to distance, the vehicle's position over the ground and the relative ocean velocity from the upward-looking ADCP are combined to calculate the distance through water, projected onto the crosswind direction. Figure 16 shows the observed temperature relative to the crosswind distance, along with the backscatter intensity from the echo sounder. Before the wind event, a shallow diurnal warm layer <1 m deep forms as a result of daytime solar heating, with small lateral gradients in temperature, and active mixing throughout, as indicated by the uniform backscatter intensity from the shallow thermocline to the surface.

During the wind event and deepening of the boundary layer, cell-like temperature structures are seen, with a spacing of about 5 m and vertical extent of around 2.5 m, consistent with pairs of LC vortices. Here, we expect downwelling regions to be associated with positive temperature anomalies of warm diurnal water, while cold anomalies upwell water from the base of the boundary layer. Note that this pattern is opposite to that observed from the surface, where temperature patterns are set by LCs interacting with the cool skin. The echo sounder reveals patterns of bubble entrainment up to about 2-m depth, much deeper than would be expected from only wave-breaking entrainment at 3 m s$^{-1}$ wind speeds, indicating regions of active downwelling due to LCs (Zedel and Farmer 1991; Osborn et al. 1992; Gemmrich and Farmer 1999; Thorpe et al. 2003b,a). While some downwelling regions are coincident with temperature maxima, the correlation is not absolute, suggesting that temperature cells could be left over from previous mixing, while new downwelling regions can appear without having yet developed a temperature signature.

Finally, toward the end of the deepening period, temperature structures have broadened and deepened to reach 8-m depth. Bubble entrainment streaks are narrower and shallower than the temperature cells, limited by the bubble's buoyancy (Thorpe et al. 2003a). Horizontal wavenumber spectra of temperature from the T-chain record were computed, but because the glider's heading is at an angle relative to the LC orientation and because it frequently changes, the evolution of scales with time could not be decomposed into components to compare with surface IR spectra.

### c. *Comparison with LES forced from observations*

The realistic model run is initialized with vertical profiles of observed temperature and demeaned horizontal velocity at 1200 UTC 20 November using basin representative profiles obtained from Wirewalker and FastCTD observations. Figure 17 shows profiles of LES temperature and velocity at 1500 UTC after a 3-h spinup. Surface wind stress and buoyancy forcing are set by observations from wave glider *Planck* (Fig. 2), while wave forcing is included through a parameterized Stokes drift profile based on the observed wind friction (Fig. 4). Again, radiative heating was applied only at the top grid cell by setting the surface heat flux equal to the total heat flux $Q_0$. As a result, the modeled surface warm layer is warmer and more strongly stratified during daytime solar heating than can be resolved from the observations (Fig. 18). An attempt to reduce incoming radiation using a scale factor of 0.63 resulted in near-surface temperature and stratification values that agreed better with observations, but the approach was rejected because DWL deepening rates diverged from observations, possibly due to the earlier onset of convective instability.

The LES initialized and forced from observations reproduces the formation of a diurnal warm layer which deepens toward the afternoon during the increase in wind forcing (Fig. 19). Weak wind forcing drives a mean flow confined to the diurnal warm layer, known as a diurnal jet (Hughes et al. 2020). The observed values of near-critical Richardson number suggest that shear instability driven by the mean flow contributes to diurnal warm layer deepening (Gargett et al. 2014; Hughes et al. 2020). The LES shows local values of enhanced shear instability at the base of LCs (Fig. 16), supporting previous studies of LCs enhancing shear-driven mixing through the downward transport of horizontal momentum (Kukulka et al. 2010).

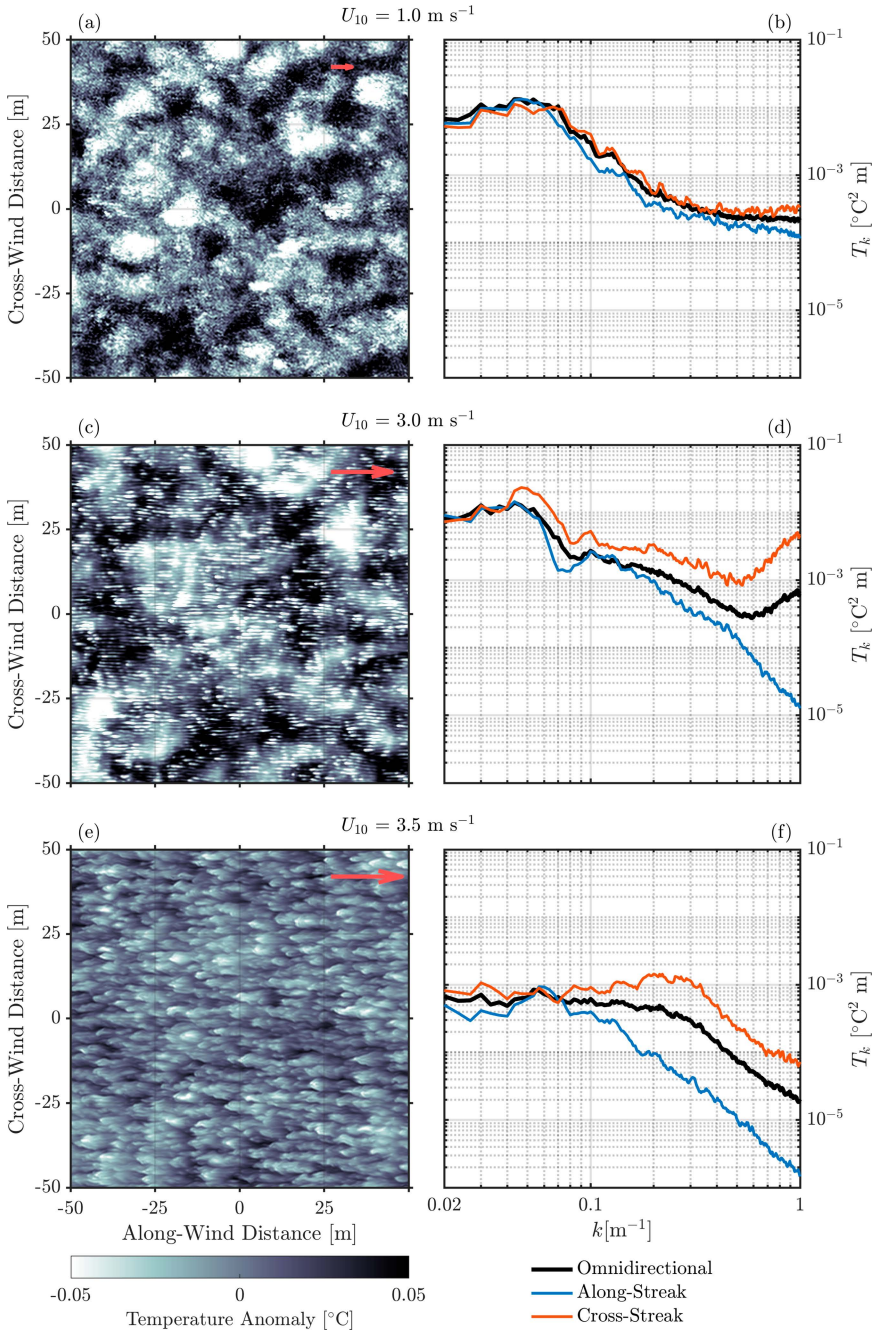


FIG. 13. (a),(c),(e) Representative samples of surface temperature from the idealized LES and (b),(d),(f) the corresponding temperature wavenumber spectra, with omnidirectional, along-cell, and cross-cell components. Note that the color map has been inverted relative to plots of observed surface temperature to preserve the interpretation of dark areas being associated with downwelling. Temperature anomaly is relative to the 2D plane fit of temperature in each panel. Wind forcing is oriented in the positive $x$ direction.

As in the idealized LES run, LC-like streaks appear here at the onset of wind forcing and grow in scale with sustained winds and boundary layer deepening (Fig. 15c). The enhanced temperature variance at small scales relative to observations might be due to insufficient model dissipation or resolution limitations in aircraft data. Subsurface, modeled temperature structures are similar to observations, with downwelling velocity collocated with temperature maxima and TKE maxima at the base of these structures. As surface buoyancy flux weakens and becomes convectively destabilizing, the LES

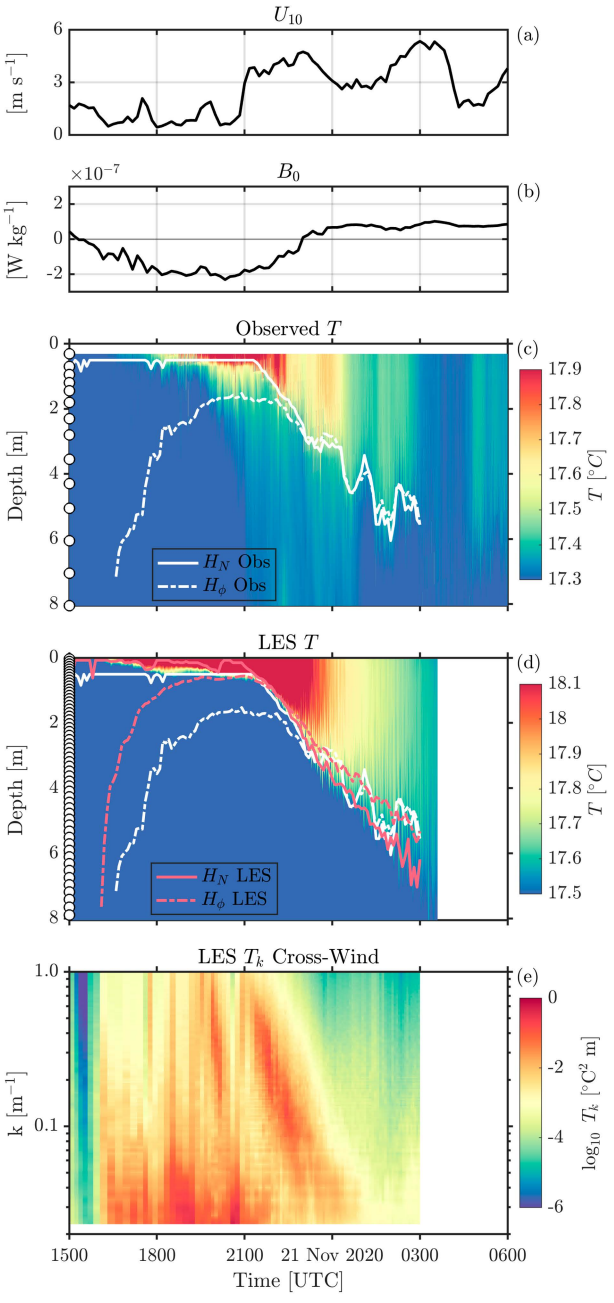


FIG. 14. Observed (a) 10-m wind speed and (b) surface buoyancy flux. (c) The evolution of temperature in the boundary layer as seen by wave glider *Planck* compared to (d) LES at its center point. (e) LES crosswind surface temperature wavenumber spectrogram. The temperature range is 0.6°C in both (c) and (d). The solid (dashed) line indicates the depth of the maximum stratification (depth of $\phi = 0.3$ J m$^{-1}$) with a 1-h moving mean for the observations (white) and LES (red). Thermistor spacing in observations and grid spacing in LES is indicated with white circles on the $y$ axis.

experiences an abrupt shift in the subsurface temperature structure at 2335 UTC (not shown), which we attribute to overly active convection in the model. As a result, by the time of the second flight, the LES surface temperature showed patterns of convective turbulence, with no clear directional peak in the 2D spectrum (Figs. 15e,f). Subsurface, downwelling regions are now associated with negative temperature anomalies, with enhanced TKE confined to near the surface.

Following the methodology to identify LC scales from horizontal temperature spectra of SST in the previous section, we compute the evolution of LC scales in the crosswind direction from snapshots of the LES at the top grid cell. The peak of the crosswind spectrum grows from 2- to 10-m scales over an hour and a half, during which time the wind was steady at around 4 m s$^{-1}$ (Fig. 14e). Over the same period, the total temperature variance also decayed by about an order of magnitude due to turbulent mixing.

### *d. Subsurface observations of full mixed layer depth LCs*

The observations and numerical simulations discussed so far are focused on relatively weak wind and wave forcing conditions, with a shallow warm layer which sets the stratification for the LC mechanics. In contrast, most prior observational studies of Langmuir circulations have focused on stronger wind forcing events with deep mixed layers. To contextualize our results with more energetic open-ocean conditions, we compare our measurements from the Catalina basin to those from the offshore deployment. On 6 November 2020, winds increased from 8 m s$^{-1}$ to a maximum of 15 m s$^{-1}$, followed by a decay to 4 m s$^{-1}$ by 14 November. The storm generated waves, with significant wave height increasing from 2 m on 5 November to over 5 m by 8 November (not shown). The air temperature was consistently cooler than the sea surface temperature during this time, leading to predominantly destabilizing surface buoyancy forcing, except during a short daytime solar maximum. Observations made from the drifting T-chain during the offshore deployment (Fig. 20) show patterns of temperature anomalies consistent with LC signatures seen in the Catalina experiment but now extending down through nearly the full depth of the mixed layer. The dominant cell spacing is consistent with twice the mixed layer depth. The transition from stabilizing daytime surface heating in Fig. 20c to nighttime cooling in Fig. 20d shows the appearance of a negative temperature anomaly in the upper mixed layer that interrupts the vertical coherence of the temperature anomaly associated with LCs.

## 5. Summary and discussion

We present novel observations of Langmuir circulations collected simultaneously from an airborne instrument [Sea Interaction Laboratory (SIO) MASS] and autonomous surface vehicles. During a morning fetch-limited land breeze in the wind shadow of Catalina Island, with weak remote swell and stabilizing surface buoyancy forcing, we observe the appearance of LCs at wind speeds of about 1–2 m s$^{-1}$, in agreement with previous observations of conditions under which Langmuir circulations appear and diurnal warm layers begin to deepen (Weller and Price 1988; Hughes et al. 2020). A strongly stratified diurnal warm layer with a depth shallower than 0.7 m constrained LCs to appear at cross-cell separation scales of about 2 m, as determined from 2D wavenumber spectra of surface temperature.

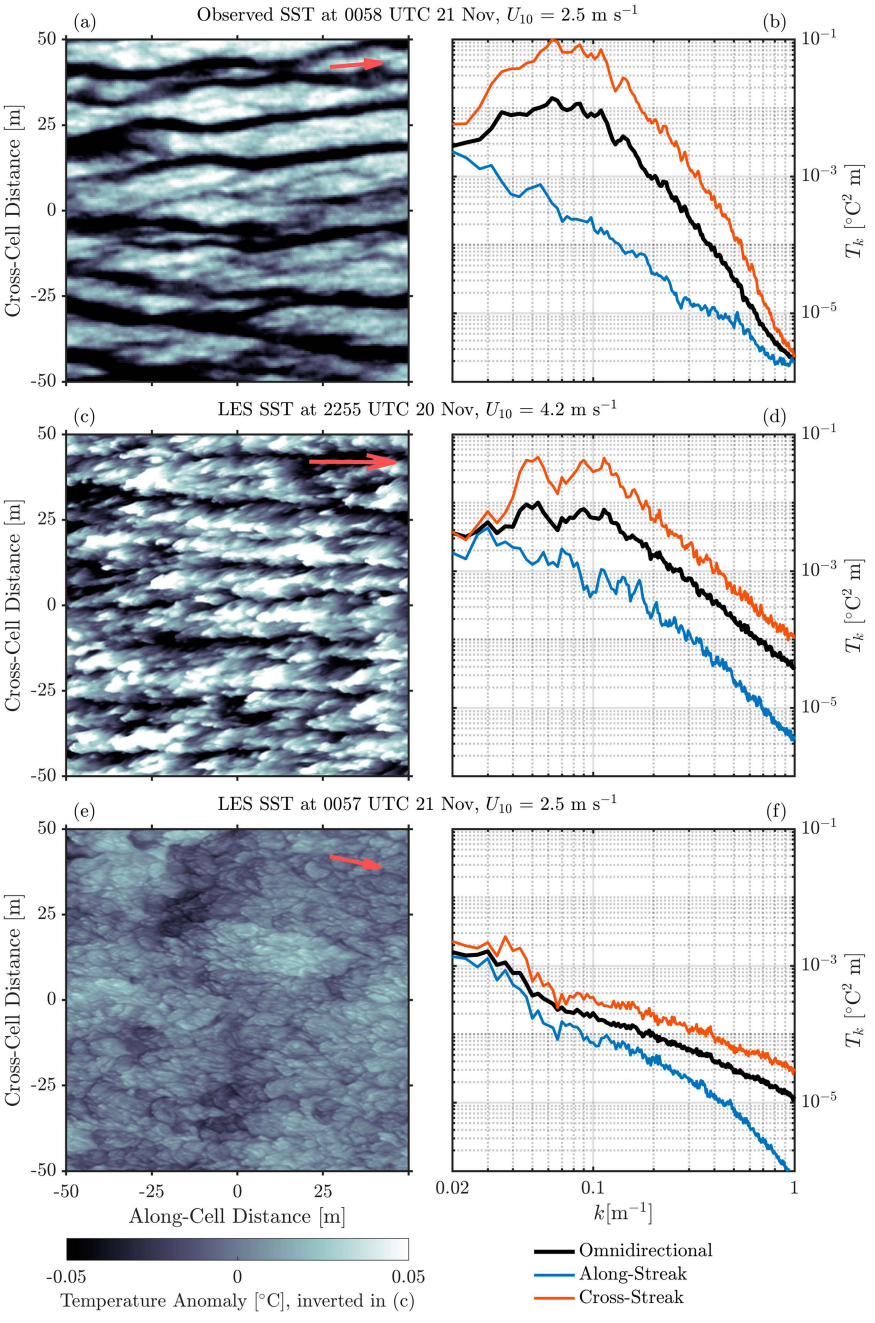


FIG. 15. (a) Surface temperature from airborne IR observations during the afternoon aircraft transects after several hours of sustained wind forcing and mixed layer deepening. LES temperature at the top grid cell, with (c) during mixed layer deepening and toward the end of stabilizing buoyancy forcing and (e) at the time of the observations in (a). (b),(d),(f) The corresponding temperature wavenumber spectra showing the omnidirectional spectrum (black), cross-cell (red), and along-cell (blue) components. Temperature anomaly is relative to the 2D plane fit of temperature in each panel. The color map in (c) has been inverted such that convergent and downwelling areas of temperature appear dark for direct comparison with cool skin observations in (a). Red arrows indicate wind, where observations in (a) use magnitude determined from the mean-square wave slope (Lenain et al. 2019) and flight-mean direction −28° obtained from nearby wave glider observations, while LES wind in (c) and (e) is set by the forcing from wave glider *Planck*.

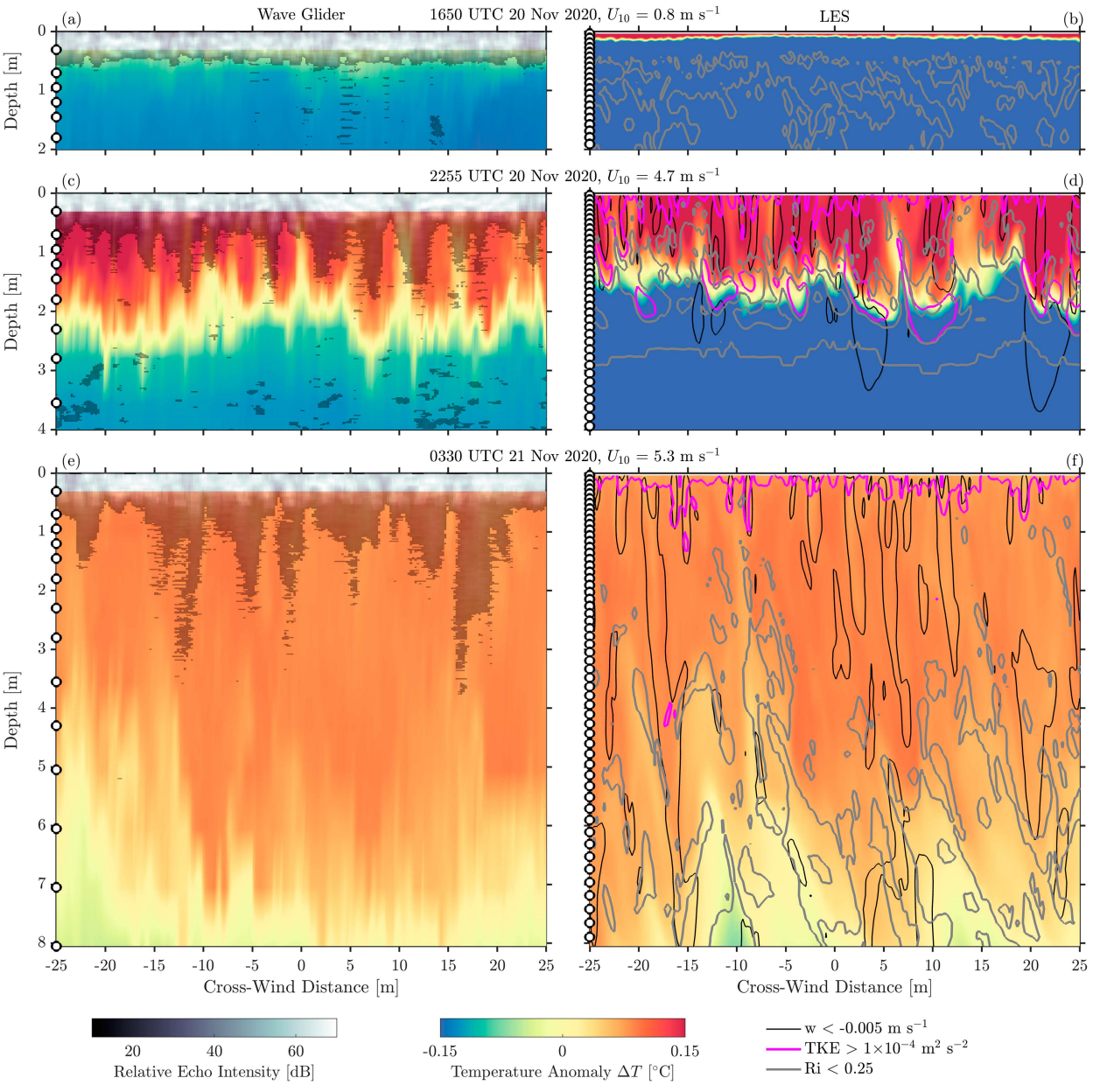


FIG. 16. (left) Wave glider temperature and echo sounder backscatter (shaded) and (right) LES temperature vs crosswind distance from (a),(b) before the wind event, (c),(d) during the wind forcing and mixed layer deepening, and (e),(f) after the wind event during the transition to convective surface cooling. Temperature colors are relative to the $y$–$z$ 2D mean temperature within the DWL. The color bar range is $\Delta T = 0.3$°C in all plots. Backscatter amplitude in echo sounder data is relative to background attenuation. A scattering signal below the boundary layer in (c) is attributable to biological scatterers. Thermistor depths are indicated on the left axis as circles. For the LES, contours of downward vertical velocity exceeding 0.005 m s$^{-1}$ are shown in black, contours of TKE exceeding $1 \times 10^{-4}$ m$^2$ s$^{-2}$ are shown in pink, and contours of Ri $< 0.25$ are shown in gray. Thermistor spacing in observations and grid spacing in LES is indicated with white circles on the $y$ axis.

The onset of LCs is nonuniform in space and is characterized by patches of relatively uniform, colder water in between regions with LCs. We hypothesize that underlying convective structures within the diurnal warm layer induce a filtering effect on the early wind wave field, excluding shorter and steeper wind waves from surface convergence zones (Longuet-Higgins 1996), thereby delaying the onset of LCs due to the reduced near-surface Stokes drift. As discussed by Wagner et al. (2023), this pattern of nonuniform LC onset suggests that wave-averaging LES models are incomplete in their treatment of LT as they cannot represent the two-way coupling between turbulent structures and surface waves.

Over several hours of consistent 2–3 m s$^{-1}$ wind forcing, we observe the deepening of the shallow surface warm layer at

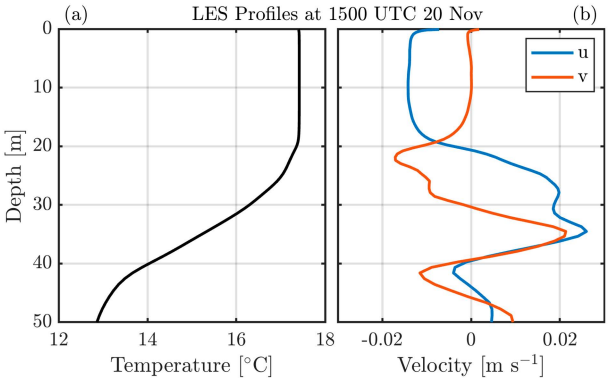


FIG. 17. LES profiles of (a) temperature and (b) horizontal velocity, after a 3-h spinup initialized from observations.

about 1 m h$^{-1}$ to 6-m depth, while LCs grow to cross-cell scales of about 15 m. Subsurface observations of temperature show cell-like patterns of warm temperature anomalies during the deepening of the diurnal warm layer. Echo sounder backscatter records show collocated patterns of bubble entrainment, roughly consistent with the spacing and scale of the temperature anomalies. As the region transitions to destabilizing buoyancy forcing, subsurface temperature anomalies become less pronounced. Patterns of bubble entrainment at the surface remain though at smaller-than-expected scales for Langmuir circulations and are no longer correlated with temperature intrusions, suggesting a transition to convective circulation. The subsurface temperature structures observed

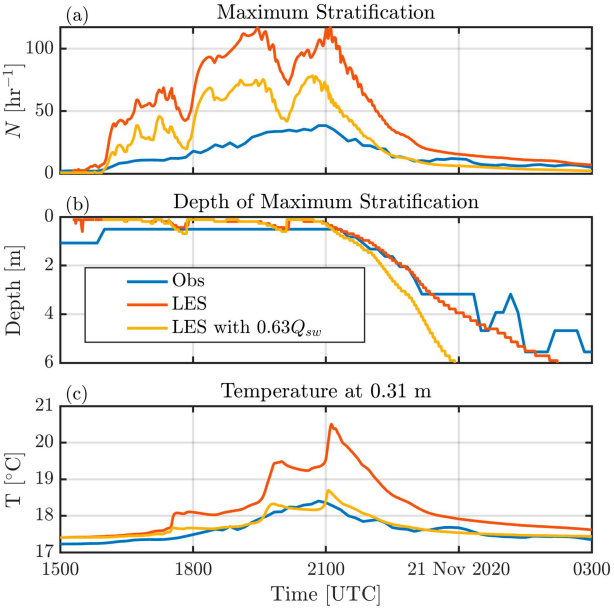


FIG. 18. (a) The maximum stratification, (b) its depth, and (c) temperature at 0.31-m depth from observations (blue), LES with single-layer heating (red), and LES with single-layer heating using shortwave flux scaled by 0.63 (yellow). Note that the observed stratification magnitude is limited by thermistor spacing, particularly near the surface, where the two thermistors nearest the surface are at 0.31- and 0.70-m depth.

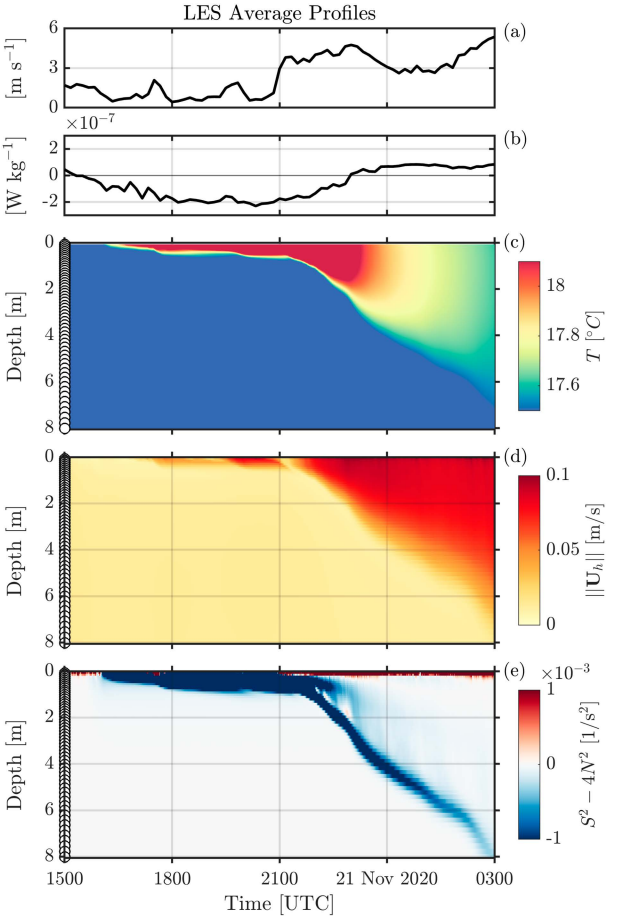


FIG. 19. LES domain-averaged (c) temperature, (d) horizontal velocity, and (e) reduced shear. Grid spacing is indicated with white circles on the $y$ axis. Forcing time series of (a) 10-m wind speed $U_{10}$ and (b) surface buoyancy flux $B_0$ are provided for reference.

during the shallow diurnal warm layer deepening are similar in character to those seen during a much stronger wind forcing event with a deep mixed layer, a regime more representative of previous observational and LES studies of LCs.

We report the observed ocean and atmospheric forcing in terms of the nondimensional scaling parameters $\mathrm{La}_{\mathrm{SL,proj}}$ and $\Lambda$ to contextualize our observations in relation to prior studies. To include Stokes drift from high-wavenumber wind waves that are not resolved with wave gliders, we expand on previous work from Pizzo et al. (2019) that parameterizes the wave spectrum from wind friction by including a calculation for the depth-dependent Stokes drift profile. Adding the Stokes drift from parameterized wind waves to the Stokes drift obtained from the observed directional wavenumber spectrum allows us to capture the rapid growth of the near-surface Stokes drift in response to wind forcing while preserving the swell contribution at depth. Numerous recent studies have addressed the impact of wind–wave misalignment and fetch limitation on the strength of LT (Wang et al. 2019; D. Wang and Kukulka 2021; X. Wang and Kukulka 2021; Wang et al. 2022). For our observations, a weak remote swell

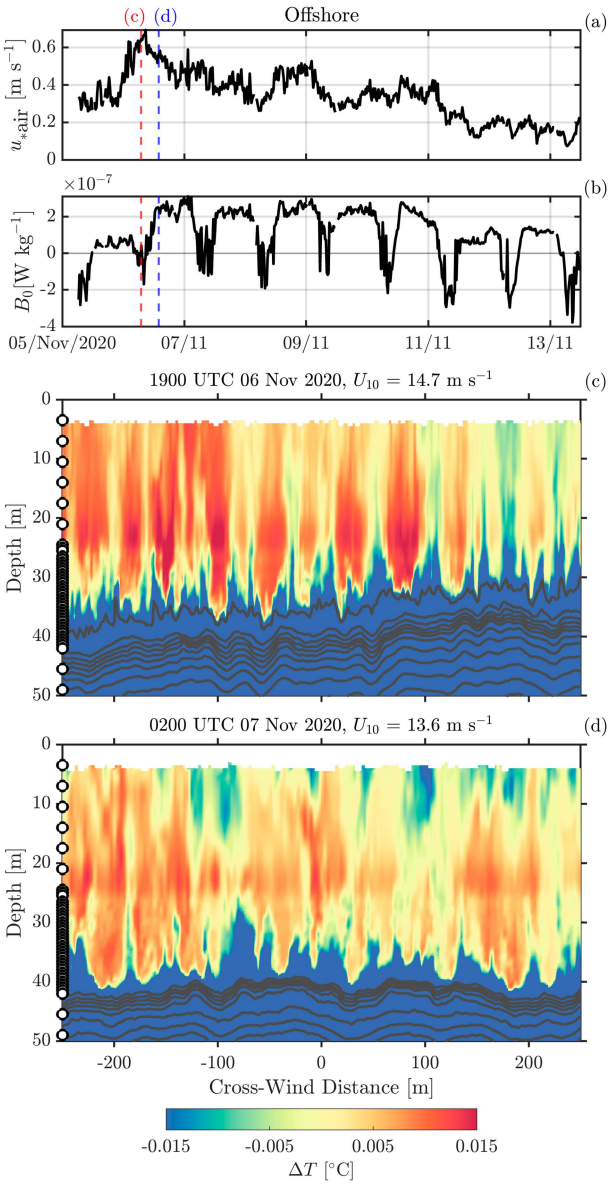


FIG. 20. Observations of LCs from the offshore thermistor chain. (a) Wind friction in the air and (b) surface buoyancy flux. (c),(d) Temperature vs depth and crosswind distance, obtained from the velocity of the drifting T-chain relative to the average mixed layer velocity from the upward-looking ADCP, scaled by the angle relative to the wind direction. The selected times in (c) and (d) are indicated by the red and blue dashed lines in the forcing time series. Thermistor spacing is indicated with white circles on the *y* axis.

meant that the dominant contribution to the surface Stokes drift came from short wind waves, even for weak wind bursts. While we use the projected surface-layer Langmuir number (Van Roekel et al. 2012), we note that its validity breaks down under conditions when wind waves oppose the remote swell, leading to an inversion of the Stokes drift shear in the surface layer. An alternative characterization of the system in the forcing space $B_0$ versus $g_*$ (Gargett 2022) reveals the large LC growth rate associated with the onset of wind forcing in the Catalina observations and relatively weaker LC growth in the offshore experiment despite the stronger wind–wave forcing.

Observations of LC appearance and growth are compared to a large-eddy simulation run with the observed meteorological and ocean forcing. The simulation reproduces the timing and rate of the diurnal warm layer deepening for the observed afternoon wind event. The general similarity in boundary layer deepening is expected for the same wind forcing due to wind-driven shear instability, with the inclusion of LT serving to enhance the deepening rate (Kukulka et al. 2010; Gargett et al. 2014). Surface temperature patterns at the onset of the wind event resemble observed LC. Due to overly active convection in the model, however, at the time of afternoon aircraft LC observations, the model surface temperature structure is dominated by convection. Subsurface temperature patterns are generally comparable to observations, and downwelling velocity patterns are comparable to the bubble entrainment signature, with the exception of large downward velocities well below the base of the diurnal warm layer. In agreement with previous studies, TKE is enhanced at the base of downwelling structures during boundary layer deepening.

An idealized run to study the onset of LCs shows their appearance at larger wind speeds and with much smaller cross-cell scales than observations. The model appears to be sensitive to the treatment of solar radiation, which inputs heat at the top grid cell, resulting in stronger DWL stratification. Attempts to reduce the solar radiation or apply a two-term solar model with distributed shortwave heat input reduced stratification but resulted in an overactive boundary layer deepening. The treatment of solar forcing in LES, particularly for shallow diurnal warm layers, requires further investigation. We caution studies of near-surface LT in LES to scrutinize the sensitivity of their models to the implementation of radiative forcing and sensitivity to convective instability.

The relation between the depth of LCs and their cross-cell spacing is important for understanding how the surface signature of Langmuir circulations relates to boundary layer dynamical processes. While our observations of cross-cell spacing versus boundary layer depth (Fig. 21) generally agree with the expected scaling of between 2 and 3 times $h$ (Smith 1992; Thorpe 2004), we also identify several important considerations to make when applying this scaling. First, in the presence of a strong diurnal warm layer, there is a large difference between the definition of the boundary layer depth that most closely relates to the dynamics of LC spacing compared to other more general mixed layer depth definitions. Our observations show the shallow diurnal warm layer deepens from $<$0.7 m to about 6 m over the course of the wind forcing, while the larger-scale mixed layer depth remained constant at about 25 m. Next, it appears that the depth defined by the maximum stratification $H_N$ better relates to the LC spacing than a definition based on the potential energy anomaly $H_\phi$. Even with a potential energy anomaly criterion tuned to reproduce the depth of the maximum stratification toward the end of the wind event, the potential energy boundary layer depth estimate overestimates the depth at the onset of deepening. At the time when LCs at 3-m scales were observed, the potential energy

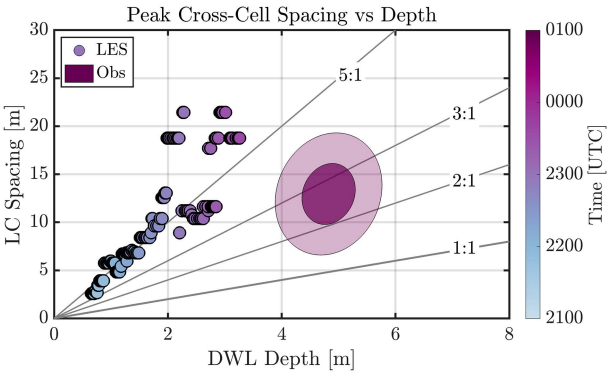


FIG. 21. The cross-cell spacing determined from spectra of sea surface temperature from LES (scattered circles) and observations (ellipse). The ellipse gives the $1\sigma$ (solid) and $2\sigma$ (light) spread of observations of cross-cell spacing from 81 images and the range of DWL depths from three subsurface wave glider T-chains at the same time. For large values of LC spacing in the LES, length scale resolution is limited by the wavenumber resolution in the spectra of temperature wavenumber. Lines trace ratios of spacing to boundary depth. LES values after 2335 UTC are omitted due to the model's overly active transition to convection.

estimate gave a boundary depth of 3 m, while the depth of maximum stratification was shallower than 1 m. Further, the ratio of cross-cell spacing appears to be sensitive to the strength of the stratification at the base of the LCs. In the limit of shallow-water full-depth Langmuir circulations, observations of cross-cell spacing of 3–10 times the water depth have been reported (Gargett et al. 2004; Marmorino et al. 2005; Gargett and Wells 2007; Kukulka et al. 2011). In our LES run, surface solar heating input at the top grid cell resulted in a stratification profile that was up to three times stronger than the observations at the onset of wind forcing. The resulting spacing of 5 times $H_N$ over the course of the DWL deepening versus the observed spacing of about 2 times might be attributable to the stronger stratification.

Another contributing factor to the wider spacing is that turbulence in the shallow diurnal warm layer is almost entirely sustained by the subgrid turbulence model. SGS models are not designed to operate when the filter scale $l > l_O$ (Sullivan et al. 2016), where the Ozmidov scale $l_O = (\epsilon/N^3)^{1/2}$ characterizes the largest eddy that has sufficient kinetic energy to overturn. For example, during the peak daytime heating regime, SGS turbulence is generated with dissipation values $\epsilon \sim 10^{-6}$ m$^2$ s$^{-3}$ and $N \sim 50$ h$^{-1}$, leading to an Ozmidov scale of $l_O < 0.04$ m, which is well below the minimum grid spacing at the surface of $\Delta = 0.2$ m. Further increasing the model resolution near the surface could improve the performance of the SGS model and therefore correct for the overly dissipative LES energetics in the upper few meters and is a topic for future work.

This work has leveraged the capability of simultaneous multiplatform observations of the OSBL to describe the onset and evolution of Langmuir circulations. These observations offer a benchmark for future LES studies that aim to improve the representation of coherent temperature structures. The relation between diurnal warm layer stratification, coherent LC spacing, deepening rates, and LT strength across a variety of forcing regimes remains unresolved and should be explored in future studies.

*Acknowledgments.* Thank you to everyone at the Multiscale Ocean Dynamics group, the Air-Sea Interaction Laboratory, the Coastal Observing Research and Development Center, and the groups of William Hodgkiss and Bill Kuperman, as well as the crews of the R/V *Sally Ride* and the R/V *Bob and Betty Beyster* for the data collected during the TFO 2020 observational campaign. The illustrative schematic was produced by Jennifer Matthews. Thanks to Jerry Smith, Sutanu Sarkar, Nick Pizzo, Baylor Fox-Kemper, Bethan Wynne-Cattanach, and Pascal Polonik for guidance and productive discussions about the research. Two reviewers, an anonymous reviewer and Ann Gargett, provided constructive and instructional comments that greatly improved this paper. This research was supported by grants from ONR (N00014-19-1-2635) and NSF (OCE; Grant OCE-2219752 for L. L.).

*Data availability statement.* All presented data are available at the UCSD Library Digital Collections (Andriatis et al. 2024) (https://doi.org/10.6075/J0VQ32W2).

## APPENDIX A

### 2d Temperature Wavenumber Spectra and LC Scales

To create temperature wavenumber spectra, composite IR images and $x$–$y$ LES temperature fields are 2D Fourier transformed using 50-m square segments with 50% overlap, Hann windows, and zero padding. A sample of the 2D Fourier transform of the IR image of Fig. 8c is shown in Fig. A1. To find the orientation of the Langmuir cells, the

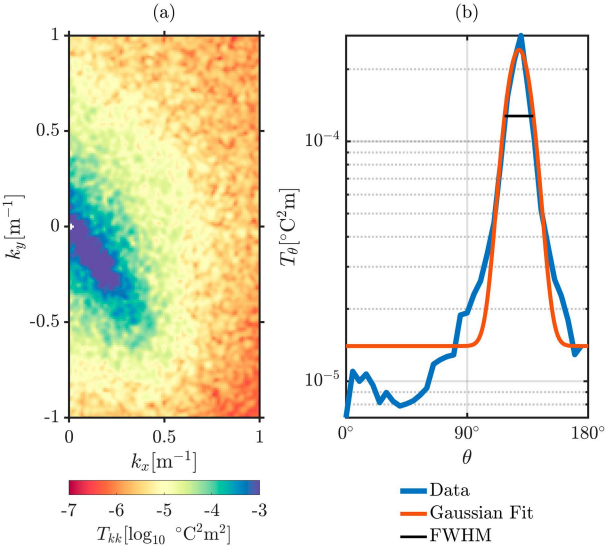


FIG. A1. (a) 2D spectrum of an IR image with Langmuir cells (Fig. 8c). (b) Radial average of the 2D spectrum between 1- and 50-m length scales, in 5° bins, with a Gaussian fit.

radial-average particle size distribution (PSD) is made using 5° bins, averaging over wavelengths from 1 to 50 m. A Gaussian is fit to the radial average, with the prominence of the Gaussian peak giving a measure of the relative LC signature, while the width gives a measure of the directional certainty. For segments with prominent LCs, the peak in the spectrum has a definite direction, while the absence of LCs results in isotropically distributed variance. To emphasize the scale of Langmuir circulations, an angular average of the directional spectrum is taken in the cross-wave direction, as defined by the peak direction of the Gaussian fit ± the full width at half maximum (FWHM), and compared to the angular average in the along-wave direction and the omnidirectional spectrum (Figs. 8b,d,f). The normal to the cross-cell direction fit is also used to reconstruct the wind direction for Fig. 6, assuming that LCs are oriented along-wind.

## APPENDIX B

### Time Series of Scaling Parameters

Time series of the scaling parameters plotted in Fig. 5 are provided in Fig. B1 for reference.

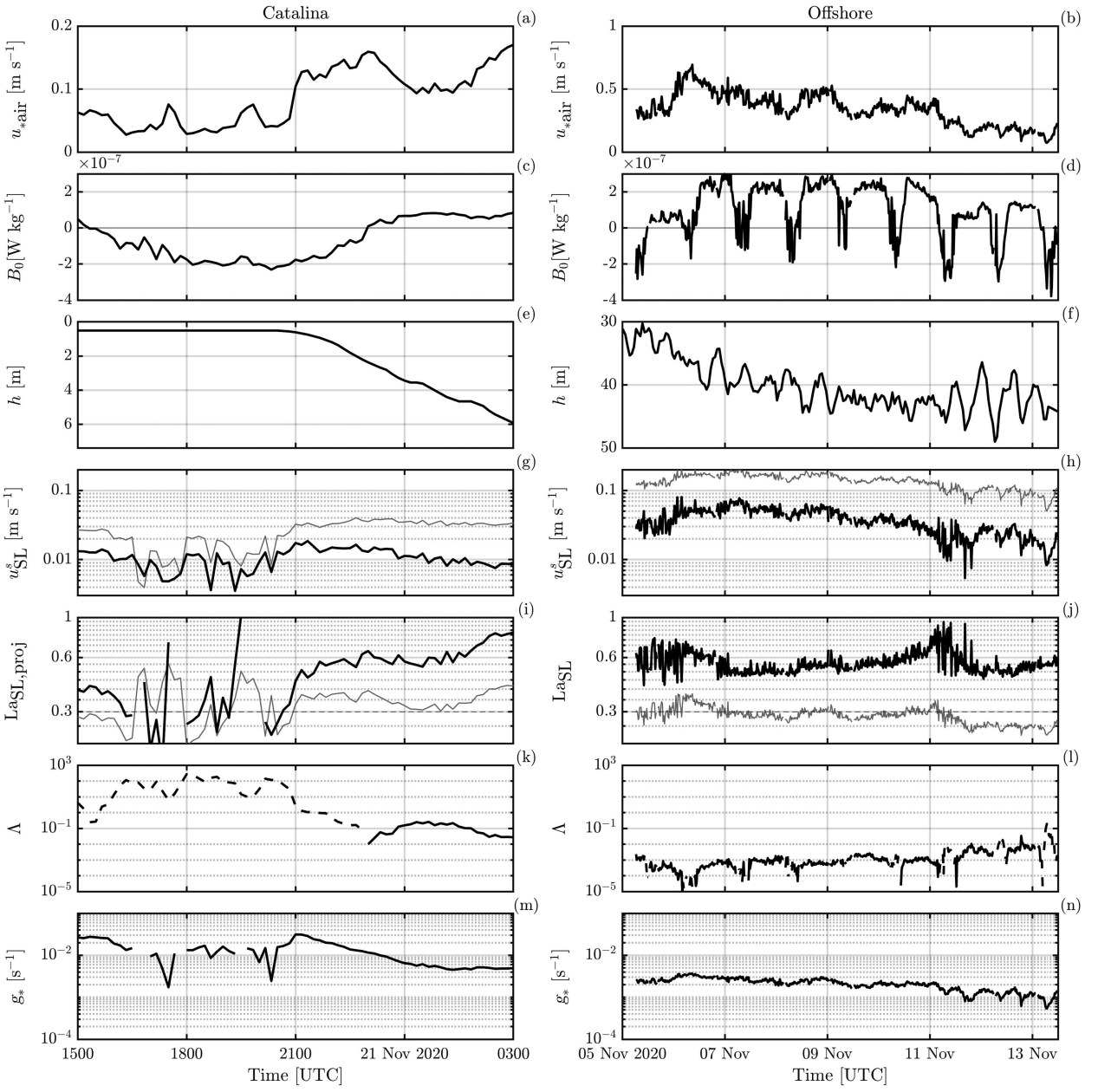


FIG. B1. Scale analysis of the forcing in (left) the Catalina basin and (right) the offshore experiment. (a),(b) Wind friction velocity in air $u_{*air}$. (c),(d) Surface buoyancy flux $B_0$. (e),(f) Boundary layer depth $h$. (g),(h) Surface-layer Stokes drift $u^s_{SL}$ (black) and surface Stokes drift $u_{s0}$ (gray). (i),(j) Surface-layer projected turbulent Langmuir number $La_{SL,proj}$ (black) and $La_t$ (gray). (k),(l) Stability parameter $\Lambda$, with periods of stabilizing forcing ($\Lambda > 0$) shown as a dashed line. (m),(n) LC growth time scale $g_*$.

## REFERENCES


Ali, A., K. H. Christensen, Ø. Breivik, M. Malila, R. P. Raj, L. Bertino, E. P. Chassignet, and M. Bakhoday-Paskyabi, 2019: A comparison of Langmuir turbulence parameterizations and key wave effects in a numerical model of the North Atlantic and Arctic Oceans. *Ocean Modell.*, **137**, 76–97, https://doi.org/10.1016/j.ocemod.2019.02.005.

Andriatis, A., L. Lenain, M. H. Alford, N. Winstead, and J. Geiman, 2024: Data from: Observations and Numerical Simulations of the Onset and Growth of Langmuir Circulations. UC San Diego Library Digital Collections, https://doi.org/10.6075/J0VQ32W2

Beare, R. J., and Coauthors, 2006: An intercomparison of large-eddy simulations of the stable boundary layer. *Bound.-Layer Meteor.*, **118**, 247–272, https://doi.org/10.1007/s10546-004-2820-6.

Belcher, S. E., and Coauthors, 2012: A global perspective on Langmuir turbulence in the ocean surface boundary layer. *Geophys. Res. Lett.*, **39**, L18605, https://doi.org/10.1029/2012GL052932.

Breivik, Ø., and K. H. Christensen, 2020: A combined stokes drift profile under swell and wind sea. *J. Phys. Oceanogr.*, **50**, 2819–2833, https://doi.org/10.1175/JPO-D-20-0087.1.

——, P. A. E. M. Janssen, and J.-R. Bidlot, 2014: Approximate stokes drift profiles in deep water. *J. Phys. Oceanogr.*, **44**, 2433–2445, https://doi.org/10.1175/JPO-D-14-0020.1.

——, J.-R. Bidlot, and P. A. E. M. Janssen, 2016: A stokes drift approximation based on the Phillips spectrum. *Ocean Modell.*, **100**, 49–56, https://doi.org/10.1016/j.ocemod.2016.01.005.

Chang, H., and Coauthors, 2019: Small-scale dispersion in the presence of Langmuir circulation. *J. Phys. Oceanogr.*, **49**, 3069–3085, https://doi.org/10.1175/JPO-D-19-0107.1.

Chini, G. P., and S. Leibovich, 2003: Resonant Langmuir-circulation–internal-wave interaction. Part I. Internal wave reflection. *J. Fluid Mech.*, **495**, 35–55, https://doi.org/10.1017/S0022112003006074.

Chor, T., J. C. McWilliams, and M. Chamecki, 2021: Modifications to the *K*-profile parameterization with nondiffusive fluxes for Langmuir turbulence. *J. Phys. Oceanogr.*, **51**, 1503–1521, https://doi.org/10.1175/JPO-D-20-0250.1.

Ciappa, A., and L. Pietranera, 2013: High resolution observations of the Terra Nova Bay polynya using COSMO-SkyMed X-SAR and other satellite imagery. *J. Mar. Syst.*, **113–114**, 42–51, https://doi.org/10.1016/j.jmarsys.2012.12.004.

Colosi, L., N. Pizzo, L. Grare, N. Statom, and L. Lenain, 2023: Observations of surface gravity wave spectra from moving platforms. *J. Atmos. Oceanic Technol.*, **40**, 1153–1169, https://doi.org/10.1175/JTECH-D-23-0022.1.

Cózar, A., S. Aliani, O. C. Basurko, M. Arias, A. Isobe, K. Topouzelis, A. Rubio, and C. Morales-Caselles, 2021: Marine litter windrows: A strategic target to understand and manage the ocean plastic pollution. *Front. Mar. Sci.*, **8**, 571796, https://doi.org/10.3389/fmars.2021.571796.

Craik, A. D. D., and S. Leibovich, 1976: A rational model for Langmuir circulations. *J. Fluid Mech.*, **73**, 401–426, https://doi.org/10.1017/S0022112076001420.

Cronin, M., and J. Sprintall, 2009: Wind-and buoyancy-forced upper ocean. *Elements of Physical Oceanography: A derivative of the Encyclopedia of Ocean Sciences*, J. H. Steele, S. A. Thorpe, and K. K. Turekian, Eds., Elsevier, Academic Press, 237–245.

D'Asaro, E. A., J. Thomson, A. Y. Shcherbina, R. R. Harcourt, M. F. Cronin, M. A. Hemer, and B. Fox-Kemper, 2014: Quantifying upper ocean turbulence driven by surface waves. *Geophys. Res. Lett.*, **41**, 102–107, https://doi.org/10.1002/2013GL058193.

Deardorff, J. W., 1970: A numerical study of three-dimensional turbulent channel flow at large Reynolds numbers. *J. Fluid Mech.*, **41**, 453–480, https://doi.org/10.1017/S0022112070000691.

de Boyer Montégut, C., G. Madec, A. S. Fischer, A. Lazar, and D. Iudicone, 2004: Mixed layer depth over the global ocean: An examination of profile data and a profile-based climatology. *J. Geophys. Res.*, **109**, C12003, https://doi.org/10.1029/2004JC002378.

Dierssen, H. M., A. Chlus, and B. Russell, 2015: Hyperspectral discrimination of floating mats of seagrass wrack and the macroalgae *Sargassum* in coastal waters of Greater Florida Bay using airborne remote sensing. *Remote Sens. Environ.*, **167**, 247–258, https://doi.org/10.1016/j.rse.2015.01.027.

Dorrell, R. M., and Coauthors, 2022: Anthropogenic mixing in seasonally stratified shelf seas by offshore wind farm infrastructure. *Front. Mar. Sci.*, **9**, 830927, https://doi.org/10.3389/fmars.2022.830927.

Drucker, R., S. Martin, and R. Moritz, 2003: Observations of ice thickness and frazil ice in the St. Lawrence Island polynya from satellite imagery, upward looking sonar, and salinity/temperature moorings. *J. Geophys. Res.*, **108**, 3149, https://doi.org/10.1029/2001JC001213.

Fairall, C. W., E. F. Bradley, J. E. Hare, A. A. Grachev, and J. B. Edson, 2003: Bulk parameterization of air and sea fluxes: Updates and verification for the COARE algorithm. *J. Climate*, **16**, 571–591, https://doi.org/10.1175/1520-0442(2003)016<0571:BPOASF>2.0.CO;2.

Fan, Y., and Coauthors, 2020: The effect of Langmuir turbulence under complex real oceanic and meteorological forcing. *Ocean Modell.*, **149**, 101601, https://doi.org/10.1016/j.ocemod.2020.101601.

Farmer, D., and M. Li, 1995: Patterns of bubble clouds organized by Langmuir circulation. *J. Phys. Oceanogr.*, **25**, 1426–1440, https://doi.org/10.1175/1520-0485(1995)025<1426:POBCOB>2.0.CO;2.

Fox-Kemper, B., L. Johnson, and F. Qiao, 2022: Ocean near-surface layers. *Ocean Mixing*, Elsevier, 65–94, https://doi.org/10.1016/b978-0-12-821512-8.00011-6.

Gargett, A., J. Wells, A. E. Tejada-Martínez, and C. E. Grosch, 2004: Langmuir supercells: A mechanism for sediment resuspension and transport in shallow seas. *Science*, **306**, 1925–1928, https://doi.org/10.1126/science.1100849.

——, D. Savidge, and J. Wells, 2014: Anatomy of a Langmuir supercell event. *J. Mar. Res.*, **72**, 127–163, https://doi.org/10.1357/002224014814901976.

Gargett, A. E., 2022: Forcing space: An alternative to regime diagrams for predicting characteristics of turbulence in the ocean surface mixing layer. *J. Phys. Oceanogr.*, **52**, 519–535, https://doi.org/10.1175/JPO-D-21-0145.1.

——, and J. R. Wells, 2007: Langmuir turbulence in shallow water. Part I. Observations. *J. Fluid Mech.*, **576**, 27–61, https://doi.org/10.1017/S0022112006004575.

——, and C. E. Grosch, 2014: Turbulence process domination under the combined forcings of wind stress, the Langmuir vortex force, and surface cooling. *J. Phys. Oceanogr.*, **44**, 44–67, https://doi.org/10.1175/JPO-D-13-021.1.

Gemmrich, J. R., and D. M. Farmer, 1999: Near-surface turbulence and thermal structure in a wind-driven sea. *J. Phys. Oceanogr.*, **29**, 480–499, https://doi.org/10.1175/1520-0485(1999)029<0480:NSTATS>2.0.CO;2.

Grant, A. L. M., and S. E. Belcher, 2009: Characteristics of Langmuir turbulence in the ocean mixed layer. *J. Phys. Oceanogr.*, **39**, 1871–1887, https://doi.org/10.1175/2009JPO4119.1.

Grare, L., N. M. Statom, N. Pizzo, and L. Lenain, 2021: Instrumented wave gliders for air-sea interaction and upper ocean research. *Front. Mar. Sci.*, **8**, 664728, https://doi.org/10.3389/fmars.2021.664728.

Harcourt, R. R., and E. A. D'Asaro, 2008: Large-eddy simulation of Langmuir turbulence in pure wind seas. *J. Phys. Oceanogr.*, **38**, 1542–1562, https://doi.org/10.1175/2007JPO3842.1.

Hodges, B. A., L. Grare, B. Greenwood, K. Matsuyoshi, N. Pizzo, N. M. Statom, J. T. Farrar, and L. Lenain, 2023: Evaluation of ocean currents observed from autonomous surface vehicles. *J. Atmos. Oceanic Technol.*, **40**, 1121–1136, https://doi.org/10.1175/JTECH-D-23-0066.1.

Hughes, K. G., J. N. Moum, and E. L. Shroyer, 2020: Evolution of the velocity structure in the diurnal warm layer. *J. Phys.*

*Oceanogr.*, **50**, 615–631, https://doi.org/10.1175/JPO-D-19-0207.1.

Johnson, L., B. Fox-Kemper, Q. Li, H. T. Pham, and S. Sarkar, 2023: A finite-time ensemble method for mixed layer model comparison. *J. Phys. Oceanogr.*, **53**, 2211–2230, https://doi.org/10.1175/JPO-D-22-0107.1.

Kenyon, K. E., 1969: Stokes drift for random gravity waves. *J. Geophys. Res.*, **74**, 6991–6994, https://doi.org/10.1029/JC074i028p06991.

Klymak, J. M., R. Pinkel, and L. Rainville, 2008: Direct breaking of the internal tide near topography: Kaena ridge, Hawaii. *J. Phys. Oceanogr.*, **38**, 380–399, https://doi.org/10.1175/2007JPO3728.1.

Kukulka, T., A. J. Plueddemann, J. H. Trowbridge, and P. P. Sullivan, 2009: Significance of Langmuir circulation in upper ocean mixing: Comparison of observations and simulations. *Geophys. Res. Lett.*, **36**, L10603, https://doi.org/10.1029/2009GL037620.

——, ——, ——, and ——, 2010: Rapid mixed layer deepening by the combination of Langmuir and shear instabilities: A case study. *J. Phys. Oceanogr.*, **40**, 2381–2400, https://doi.org/10.1175/2010JPO4403.1.

——, ——, ——, and ——, 2011: The influence of crosswind tidal currents on Langmuir circulation in a shallow ocean. *J. Geophys. Res.*, **116**, C08005, https://doi.org/10.1029/2011JC006971.

——, ——, and P. P. Sullivan, 2013: Inhibited upper ocean restratification in nonequilibrium swell conditions. *Geophys. Res. Lett.*, **40**, 3672–3676, https://doi.org/10.1002/grl.50708.

Langmuir, I., 1938: Surface motion of water induced by wind. *Science*, **87**, 119–123, https://doi.org/10.1126/science.87.2250.119.

Large, W. G., J. C. McWilliams, and S. C. Doney, 1994: Oceanic vertical mixing: A review and a model with a nonlocal boundary layer parameterization. *Rev. Geophys.*, **32**, 363–403, https://doi.org/10.1029/94RG01872.

Larson, K. J., 1992: Riding Langmuir circulations and swimming in circles: A novel form of clustering behavior by the scyphomedusa *Linuche unguiculata*. *Mar. Biol.*, **112**, 229–235, https://doi.org/10.1007/BF00702466.

Lenain, L., and W. K. Melville, 2017: Measurements of the directional spectrum across the equilibrium saturation ranges of wind-generated surface waves. *J. Phys. Oceanogr.*, **47**, 2123–2138, https://doi.org/10.1175/JPO-D-17-0017.1.

——, and N. Pizzo, 2020: The contribution of high-frequency wind-generated surface waves to the stokes drift. *J. Phys. Oceanogr.*, **50**, 3455–3465, https://doi.org/10.1175/JPO-D-20-0116.1.

——, N. M. Statom, and W. K. Melville, 2019: Airborne measurements of surface wind and slope statistics over the ocean. *J. Phys. Oceanogr.*, **49**, 2799–2814, https://doi.org/10.1175/JPO-D-19-0098.1.

Li, M., K. Zahariev, and C. Garrett, 1995: Role of Langmuir circulation in the deepening of the ocean surface mixed layer. *Science*, **270**, 1955–1957, https://doi.org/10.1126/science.270.5244.1955.

——, C. Garrett, and E. Skyllingstad, 2005: A regime diagram for classifying turbulent large eddies in the upper ocean. *Deep-Sea Res. I*, **52**, 259–278, https://doi.org/10.1016/j.dsr.2004.09.004.

Li, Q., and B. Fox-Kemper, 2017: Assessing the effects of Langmuir turbulence on the entrainment buoyancy flux in the ocean surface boundary layer. *J. Phys. Oceanogr.*, **47**, 2863–2886, https://doi.org/10.1175/JPO-D-17-0085.1.

——, A. Webb, B. Fox-Kemper, A. Craig, G. Danabasoglu, W. G. Large, and M. Vertenstein, 2016: Langmuir mixing effects on global climate: WAVEWATCH III in CESM. *Ocean Modell.*, **103**, 145–160, https://doi.org/10.1016/j.ocemod.2015.07.020.

——, B. Fox-Kemper, Ø. Breivik, and A. Webb, 2017: Statistical models of global Langmuir mixing. *Ocean Modell.*, **113**, 95–114, https://doi.org/10.1016/j.ocemod.2017.03.016.

——, and Coauthors, 2019: Comparing ocean surface boundary vertical mixing schemes including Langmuir turbulence. *J. Adv. Model. Earth Syst.*, **11**, 3545–3592, https://doi.org/10.1029/2019MS001810.

Longuet-Higgins, M. S., 1996: Surface manifestations of turbulent flow. *J. Fluid Mech.*, **308**, 15–29, https://doi.org/10.1017/S0022112096001371.

Marmorino, G. O., G. B. Smith, and G. J. Lindemann, 2005: Infrared imagery of large-aspect-ratio Langmuir circulation. *Cont. Shelf Res.*, **25** (1), 1–6, https://doi.org/10.1016/j.csr.2004.08.002.

——, J. V. Toporkov, G. B. Smith, M. A. Sletten, D. Perkovic, S. Frasier, and K. P. Judd, 2007: Ocean mixed-layer depth and current variation estimated from imagery of surfactant streaks. *IEEE Geosci. Remote Sens. Lett.*, **4**, 364–367, https://doi.org/10.1109/LGRS.2007.895702.

——, G. B. Smith, J. V. Toporkov, M. A. Sletten, D. Perkovic, and S. J. Frasier, 2008: Evolution of ocean slicks under a rising wind. *J. Geophys. Res.*, **113**, C04030, https://doi.org/10.1029/2007JC004538.

McWilliams, J. C., and P. P. Sullivan, 2000: Vertical mixing by Langmuir circulations. *Spill Sci. Technol. Bull.*, **6**, 225–237, https://doi.org/10.1016/S1353-2561(01)00041-X.

——, ——, and C.-H. Moeng, 1997: Langmuir turbulence in the ocean. *J. Fluid Mech.*, **334**, 1–30, https://doi.org/10.1017/S0022112096004375.

——, E. Huckle, J. Liang, and P. P. Sullivan, 2014: Langmuir turbulence in swell. *J. Phys. Oceanogr.*, **44**, 870–890, https://doi.org/10.1175/JPO-D-13-0122.1.

Melville, W. K., R. Shear, and F. Veron, 1998: Laboratory measurements of the generation and evolution of Langmuir circulations. *J. Fluid Mech.*, **364**, 31–58, https://doi.org/10.1017/S0022112098001098.

——, L. Lenain, D. R. Cayan, M. Kahru, J. P. Kleissl, P. F. Linden, and N. M. Statom, 2016: The modular aerial sensing system. *J. Atmos. Oceanic Technol.*, **33**, 1169–1184, https://doi.org/10.1175/JTECH-D-15-0067.1.

Min, H. S., and Y. Noh, 2004: Influence of the surface heating on Langmuir circulation. *J. Phys. Oceanogr.*, **34**, 2630–2641, https://doi.org/10.1175/JPOJPO-2654.1.

Moeng, C.-H., 1984: A large-eddy-simulation model for the study of planetary boundary-layer turbulence. *J. Atmos. Sci.*, **41**, 2052–2062, https://doi.org/10.1175/1520-0469(1984)041%3C2052:ALESMF%3E2.0.CO;2.

Noh, Y., G. Goh, S. Raasch, and M. Gryschka, 2009: Formation of a diurnal thermocline in the ocean mixed layer simulated by les. *J. Phys. Oceanogr.*, **39**, 1244–1257, https://doi.org/10.1175/2008JPO4032.1.

Osborn, T., D. Farmer, S. Vagle, S. A. Thorpe, and M. Cure, 1992: Measurements of bubble plumes and turbulence from a submarine. *Atmos.–Ocean*, **30**, 419–440, https://doi.org/10.1080/07055900.1992.9649447.

Paulson, C. A., and J. J. Simpson, 1977: Irradiance measurements in the upper ocean. *J. Phys. Oceanogr.*, **7**, 952–956, https://doi.org/10.1175/1520-0485(1977)007<0952:IMITUO>2.0.CO;2.

Pearson, B. C., A. L. M. Grant, J. A. Polton, and S. E. Belcher, 2015: Langmuir turbulence and surface heating in the ocean surface boundary layer. *J. Phys. Oceanogr.*, **45**, 2897–2911, https://doi.org/10.1175/JPO-D-15-0018.1.

Pham, H. T., S. Sarkar, L. Johnson, B. Fox-Kemper, P. P. Sullivan, and Q. Li, 2023: Multi-scale temporal variability of turbulent mixing during a monsoon intra-seasonal oscillation in the Bay of Bengal: An LES study. *J. Geophys. Res. Oceans*, **128**, e2022JC018959, https://doi.org/10.1029/2022JC018959.

Pinkel, R., M. A. Goldin, J. A. Smith, O. M. Sun, A. A. Aja, M. N. Bui, and T. Hughen, 2011: The Wirewalker: A vertically profiling instrument carrier powered by ocean waves. *J. Atmos. Oceanic Technol.*, **28**, 426–435, https://doi.org/10.1175/2010JTECHO805.1.

Pizzo, N., W. K. Melville, and L. Deike, 2019: Lagrangian transport by nonbreaking and breaking deep-water waves at the ocean surface. *J. Phys. Oceanogr.*, **49**, 983–992, https://doi.org/10.1175/JPO-D-18-0227.1.

Plueddemann, A. J., J. A. Smith, D. M. Farmer, R. A. Weller, W. R. Crawford, R. Pinkel, S. Vagle, and A. Gnanadesikan, 1996: Structure and variability of Langmuir circulation during the surface waves processes program. *J. Geophys. Res.*, **101**, 3525–3543, https://doi.org/10.1029/95JC03282.

Reichl, B. G., A. Adcroft, S. M. Griffies, and R. Hallberg, 2022: A potential energy analysis of ocean surface mixed layers. *J. Geophys. Res. Oceans*, **127**, e2021JC018140, https://doi.org/10.1029/2021JC018140.

Schultz, C., S. C. Doney, W. G. Zhang, H. Regan, P. Holland, M. P. Meredith, and S. Stammerjohn, 2020: Modeling of the influence of sea ice cycle and Langmuir circulation on the upper ocean mixed layer depth and freshwater distribution at the west Antarctic Peninsula. *J. Geophys. Res. Oceans*, **125**, e2020JC016109, https://doi.org/10.1029/2020JC016109.

Simecek-Beatty, D., and W. J. Lehr, 2017: Extended oil spill spreading with Langmuir circulation. *Mar. Pollut. Bull.*, **122**, 226–235, https://doi.org/10.1016/j.marpolbul.2017.06.047.

Skyllingstad, E. D., and D. W. Denbo, 1995: An ocean large-eddy simulation of Langmuir circulations and convection in the surface mixed layer. *J. Geophys. Res.*, **100**, 8501–8522, https://doi.org/10.1029/94JC03202.

——, W. D. Smyth, and G. B. Crawford, 2000: Resonant wind-driven mixing in the ocean boundary layer. *J. Phys. Oceanogr.*, **30**, 1866–1890, https://doi.org/10.1175/1520-0485(2000)030%3C1866:RWDMIT%3E2.0.CO;2.

Smagorinsky, J., 1963: General circulation experiments with the primitive equations. *Mon. Wea. Rev.*, **91**, 99–164, https://doi.org/10.1175/1520-0493(1963)091<0099:GCEWTP>2.3.CO;2.

Smith, J. A., 1992: Observed growth of Langmuir circulation. *J. Geophys. Res.*, **97**, 5651–5664, https://doi.org/10.1029/91JC03118.

Smyth, W. D., E. D. Skyllingstad, G. B. Crawford, and H. Wijesekera, 2002: Nonlocal fluxes and stokes drift effects in the K-profile parameterization. *Ocean Dyn.*, **52**, 104–115, https://doi.org/10.1007/s10236-002-0012-9.

Solano, M., and Y. Fan, 2022: A new K-profile parameterization for the ocean surface boundary layer under realistic forcing conditions. *Ocean Modell.*, **171**, 101958, https://doi.org/10.1016/j.ocemod.2022.101958.

Sullivan, P. P., and J. C. McWilliams, 2017: Frontogenesis and frontal arrest of a dense filament in the oceanic surface boundary layer. *J. Fluid Mech.*, **837**, 341–380, https://doi.org/10.1017/jfm.2017.833.

——, ——, and W. K. Melville, 2007: Surface gravity wave effects in the oceanic boundary layer: Large-eddy simulation with vortex force and stochastic breakers. *J. Fluid Mech.*, **593**, 405–452, https://doi.org/10.1017/S002211200700897X.

——, L. Romero, J. C. McWilliams, and W. K. Melville, 2012: Transient evolution of Langmuir turbulence in ocean boundary layers driven by hurricane winds and waves. *J. Phys. Oceanogr.*, **42**, 1959–1980, https://doi.org/10.1175/JPO-D-12-025.1.

——, J. C. Weil, E. G. Patton, H. J. J. Jonker, and D. V. Mironov, 2016: Turbulent winds and temperature fronts in large-eddy simulations of the stable atmospheric boundary layer. *J. Atmos. Sci.*, **73**, 1815–1840, https://doi.org/10.1175/JAS-D-15-0339.1.

Sutherland, B. R., M. DiBenedetto, A. Kaminski, and T. van den Bremer, 2023: Fluid dynamics challenges in predicting plastic pollution transport in the ocean: A perspective. *Phys. Rev. Fluids*, **8**, 070701, https://doi.org/10.1103/PhysRevFluids.8.070701.

Sutherland, P., and W. K. Melville, 2015: Field measurements of surface and near-surface turbulence in the presence of breaking waves. *J. Phys. Oceanogr.*, **45**, 943–965, https://doi.org/10.1175/JPO-D-14-0133.1.

Teixeira, M. A. C., and S. E. Belcher, 2002: On the distortion of turbulence by a progressive surface wave. *J. Fluid Mech.*, **458**, 229–267, https://doi.org/10.1017/S0022112002007838.

Tejada-Martínez, A. E., and C. E. Grosch, 2007: Langmuir turbulence in shallow water. Part II. Large-eddy simulation. *J. Fluid Mech.*, **576**, 63–108, https://doi.org/10.1017/S0022112006004587.

Thorpe, S. A., 2004: Langmuir circulation. *Annu. Rev. Fluid Mech.*, **36**, 55–79, https://doi.org/10.1146/annurev.fluid.36.052203.071431.

——, T. R. Osborn, D. M. Farmer, and S. Vagle, 2003a: Bubble clouds and Langmuir circulation: Observations and models. *J. Phys. Oceanogr.*, **33**, 2013–2031, https://doi.org/10.1175/1520-0485(2003)033%3C2013:BCALCO%3E2.0.CO;2.

——, ——, J. F. E. Jackson, A. J. Hall, and R. G. Lueck, 2003b: Measurements of turbulence in the upper-ocean mixing layer using Autosub. *J. Phys. Oceanogr.*, **33**, 122–145, https://doi.org/10.1175/1520-0485(2003)033<0122:MOTITU>2.0.CO;2.

Van Roekel, L. P., B. Fox-Kemper, P. P. Sullivan, P. E. Hamlington, and S. R. Haney, 2012: The form and orientation of Langmuir cells for misaligned winds and waves. *J. Geophys. Res.*, **117**, C05001, https://doi.org/10.1029/2011JC007516.

Veron, F., and W. K. Melville, 2001: Experiments on the stability and transition of wind-driven water surfaces. *J. Fluid Mech.*, **446**, 25–65, https://doi.org/10.1017/S0022112001005638.

——, ——, and L. Lenain, 2008a: Infrared techniques for measuring ocean surface processes. *J. Atmos. Oceanic Technol.*, **25**, 307–326, https://doi.org/10.1175/2007JTECHO524.1.

——, ——, and ——, 2008b: Wave-coherent air–sea heat flux. *J. Phys. Oceanogr.*, **38**, 788–802, https://doi.org/10.1175/2007JPO3682.1.

——, ——, and ——, 2009: Measurements of ocean surface turbulence and wave–turbulence interactions. *J. Phys. Oceanogr.*, **39**, 2310–2323, https://doi.org/10.1175/2009JPO4019.1.

Vrećica, T., N. Pizzo, and L. Lenain, 2022: Airborne observations of shoaling and breaking internal waves. *Geophys. Res. Lett.*, **49**, e2022GL100622, https://doi.org/10.1029/2022GL100622.

Wagner, G. L., N. Pizzo, L. Lenain, and F. Veron, 2023: Transition to turbulence in wind-drift layers. *J. Fluid Mech.*, **976**, A8, https://doi.org/10.1017/jfm.2023.920.

Wang, D., and T. Kukulka, 2021: Wind- and wave-driven Reynolds stress and velocity shear in the upper ocean for idealized misaligned wind-wave conditions. *J. Phys. Oceanogr.*, **51**, 633–644, https://doi.org/10.1175/JPO-D-20-0157.1.

——, ——, B. G. Reichl, T. Hara, and I. Ginis, 2019: Wind and wave misalignment effects on Langmuir turbulence in tropical cyclone conditions. *J. Phys. Oceanogr.*, **49**, 3109–3126, https://doi.org/10.1175/JPO-D-19-0093.1.

Wang, X., and T. Kukulka, 2021: Ocean surface boundary layer response to abruptly turning winds. *J. Phys. Oceanogr.*, **51**, 1779–1794, https://doi.org/10.1175/JPO-D-20-0198.1.

——, ——, and A. J. Plueddemann, 2022: Wind fetch and direction effects on Langmuir turbulence in a coastal ocean. *J. Geophys. Res. Oceans*, **127**, e2021JC018222, https://doi.org/10.1029/2021JC018222.

——, ——, J. T. Farrar, A. J. Plueddemann, and S. F. Zippel, 2023: Langmuir turbulence controls on observed diurnal warm layer depths. *Geophys. Res. Lett.*, **50**, e2023GL103231, https://doi.org/10.1029/2023GL103231.

Webb, A., and B. Fox-Kemper, 2011: Wave spectral moments and stokes drift estimation. *Ocean Modell.*, **40**, 273–288, https://doi.org/10.1016/j.ocemod.2011.08.007.

——, and ——, 2015: Impacts of wave spreading and multidirectional waves on estimating stokes drift. *Ocean Modell.*, **96**, 49–64, https://doi.org/10.1016/j.ocemod.2014.12.007.

Weller, R. A., and J. F. Price, 1988: Langmuir circulation within the oceanic mixed layer. *Deep-Sea Res.*, **35A**, 711–747, https://doi.org/10.1016/0198-0149(88)90027-1.

——, J. P. Dean, J. F. Price, E. A. Francis, J. Marra, and D. C. Boardman, 1985: Three-dimensional flow in the upper ocean. *Science*, **227**, 1552–1556, https://doi.org/10.1126/science.227.4694.1552.

Yan, C., J. C. McWilliams, and M. Chamecki, 2021: Generation of attached Langmuir circulations by a suspended macroalgal farm. *J. Fluid Mech.*, **915**, A76, https://doi.org/10.1017/jfm.2021.111.

Zappa, C. J., and A. T. Jessup, 2005: High-resolution airborne infrared measurements of ocean skin temperature. *IEEE Geosci. Remote Sens. Lett.*, **2**, 146–150, https://doi.org/10.1109/LGRS.2004.841629.

Zedel, L., and D. Farmer, 1991: Organized structures in subsurface bubble clouds: Langmuir circulation in the open ocean. *J. Geophys. Res.*, **96**, 8889–8900, https://doi.org/10.1029/91JC00189.

Zheng, B., A. J. Lucas, R. Pinkel, and A. L. Boyer, 2022: Fine-scale velocity measurement on the Wirewalker wave-powered profiler. *J. Atmos. Oceanic Technol.*, **39**, 133–147, https://doi.org/10.1175/JTECH-D-21-0048.1.